



HAL
open science

Characterization of the Carnian Pluvial Episode in the Argana Basin (Western High Atlas, Morocco): An approach based on sedimentology, clay mineralogy and paleosols

A. Tourani, N. Benaouiss, R. de la Horra, José F Barrenechea, J F López-Gómez, O.F. Gallego, Sylvie Bourquin

► To cite this version:

A. Tourani, N. Benaouiss, R. de la Horra, José F Barrenechea, J F López-Gómez, et al.. Characterization of the Carnian Pluvial Episode in the Argana Basin (Western High Atlas, Morocco): An approach based on sedimentology, clay mineralogy and paleosols. *Palaeogeography, Palaeoclimatology, Palaeoecology*, 2023, 627, pp.111720. 10.1016/j.palaeo.2023.111720 . insu-04159643v2

HAL Id: insu-04159643

<https://insu.hal.science/insu-04159643v2>

Submitted on 17 Jul 2023

HAL is a multi-disciplinary open access archive for the deposit and dissemination of scientific research documents, whether they are published or not. The documents may come from teaching and research institutions in France or abroad, or from public or private research centers.

L'archive ouverte pluridisciplinaire **HAL**, est destinée au dépôt et à la diffusion de documents scientifiques de niveau recherche, publiés ou non, émanant des établissements d'enseignement et de recherche français ou étrangers, des laboratoires publics ou privés.



Distributed under a Creative Commons Attribution 4.0 International License



Characterization of the Carnian Pluvial Episode in the Argana Basin (Western High Atlas, Morocco): An approach based on sedimentology, clay mineralogy and paleosols

A. Tourani^a, N. Benaouiss^a, R. De la Horra^b, J.F. Barrenechea^{c,d,*}, J. López-Gómez^d, O.F. Gallego^e, S. Bourquin^f

^a Département de Géologie, Faculté des Sciences Semlalia, Université Cadi Ayyad, Boulevard Prince Moulay Abdellah, 2390 Marrakech, Morocco

^b Departamento de Geodinámica, Estratigrafía, Paleontología, Facultad de Geología, Universidad Complutense, C/ José Antonio Novais 2, 28040 Madrid, Spain

^c Departamento de Mineralogía y Petrología, Facultad de Geología, Universidad Complutense, C/ José Antonio Novais 2, 28040 Madrid, Spain

^d Instituto de Geociencias (CSIC-UCM), Universidad Complutense, C/ Severo Ochoa 7, 28040 Madrid, Spain

^e Centro de Ecología Aplicada del Litoral (CECOAL-CONICET-UNNE), y Área Ciencias de la Tierra, Dpto. Biología, Facultad de Ciencias, Exactas y Naturales y Agrimensura (FaCENA), Universidad Nacional del Nordeste (UNNE), Ruta Prov. N° 5, CP 3400 Corrientes, Argentina

^f Univ. Rennes, CNRS, Géosciences Rennes-UMR CNRS 6118, F-35000 Rennes, France

ARTICLE INFO

Editor: S Shen

Keywords:

CPE
Argana Basin
Late Triassic
Carnian
Morocco
Carnian Pluvial Episode
Clam shrimp

ABSTRACT

We report on a multi-proxy study of the Carnian Pluvial Episode in the continental Argana Basin (Morocco) based on mineralogy, geochemistry, paleosols and sedimentary features. The study focus on two sections of the Irohalene Member (unit t5) of the Timezgadiouine Formation dated as late Julian-early Tuvalian through clam shrimp (conchostracan) associations. The sedimentary study of the Irohalene Member defines three parts: lower, middle and upper (t5.1, t5.2, t5.3 respectively). The base of the lower part comprises channels with gravel and sandy bars related to proximal areas, and fluvial meandering systems, overbank and floodplain deposits developing upwards. Extensive floodplains showing the development of siliciclastic and carbonate lakes mostly represent the t5.2 and t5.3 parts, although the sedimentary characteristics of the former reflect more humid and permanent water conditions. These more humid characteristics are also indicated by the drastic change from calcareous paleosols in t5.1 to smectitic Vertisols in t5.2, which occur in relation to thin layers of lacustrine carbonates, greenish lutites, and hybrid oolitic sandstones of palustrine environments. Stable carbon and oxygen isotope data are consistent with a general tendency towards the arid conditions observed in the Tadart Ouadou t6 Member of the Bigoudine Formation, of fluvial-eolian origin and younger in age. This general tendency is interrupted by at least two humid yet hot intervals characterized by pedogenic carbonates featuring lighter isotope compositions and lacustrine carbonates precipitated under conditions of high temperatures and evaporation rates.

1. Introduction

The Late Triassic probably represented the only period of the Phanerozoic without evidence of glacial activity (Preto et al., 2010). During this period, the Tethys realm and neighboring basins mostly developed under greenhouse conditions dominated by a semi-arid warm climate interspersed with brief hot phases (Royer et al., 2004). However, a short humid episode occurred during the Julian to Tuvalian of the Carnian, recorded as a drastic change in the climate and environmental

conditions. This humid episode was described and termed the Carnian Pluvial Episode (CPE) by Simms and Ruffell (1989). The CPE was a time of major turnover in marine and terrestrial ecosystems (Dal Corso et al., 2015, 2020; Barrenechea et al., 2018), and its onset and end has been linked to significant biotic changes, including both extinctions and diversifications (Benton et al., 2014, 2018; Bernardi et al., 2018; Buffa et al., 2019). These changes resulted in a major extinction event, or even more than one (Benton, 1986), which was followed by explosive diversification of both continental and marine organisms (Dal Corso

* Corresponding author at: Departamento de Mineralogía y Petrología, Facultad de Geología, Universidad Complutense, C/ José Antonio Novais 2, 28040 Madrid, Spain.

E-mail address: barrene@ucm.es (J.F. Barrenechea).

<https://doi.org/10.1016/j.palaeo.2023.111720>

Received 22 February 2023; Received in revised form 5 July 2023; Accepted 7 July 2023

Available online 10 July 2023

0031-0182/© 2023 The Authors. Published by Elsevier B.V. This is an open access article under the CC BY license (<http://creativecommons.org/licenses/by/4.0/>).

et al., 2018, 2020). Recent studies have identified this humid episode as a global phenomenon and suggest its possible link to the Wrangellia Large Igneous Province (Furin et al., 2006; Dal Corso et al., 2012, 2015, 2018, 2020; Sun et al., 2016; Lu et al., 2021; Tomimatsu et al., 2021; Lu et al., 2021). However, while evidence exists that this pluvial episode is not reflected by a single episode but by three or four main episodes in

both marine (Breda et al., 2009; Stefani et al., 2010; Franz et al., 2014; Roghi et al., 2010; Sun et al., 2016; Dal Corso et al., 2018) and continental records (Arche and López-Gómez, 2014; Barrenechea et al., 2018), little is known about the relationships between these pulses in marine and continental domains.

The CPE represents a relatively short time-interval spanning

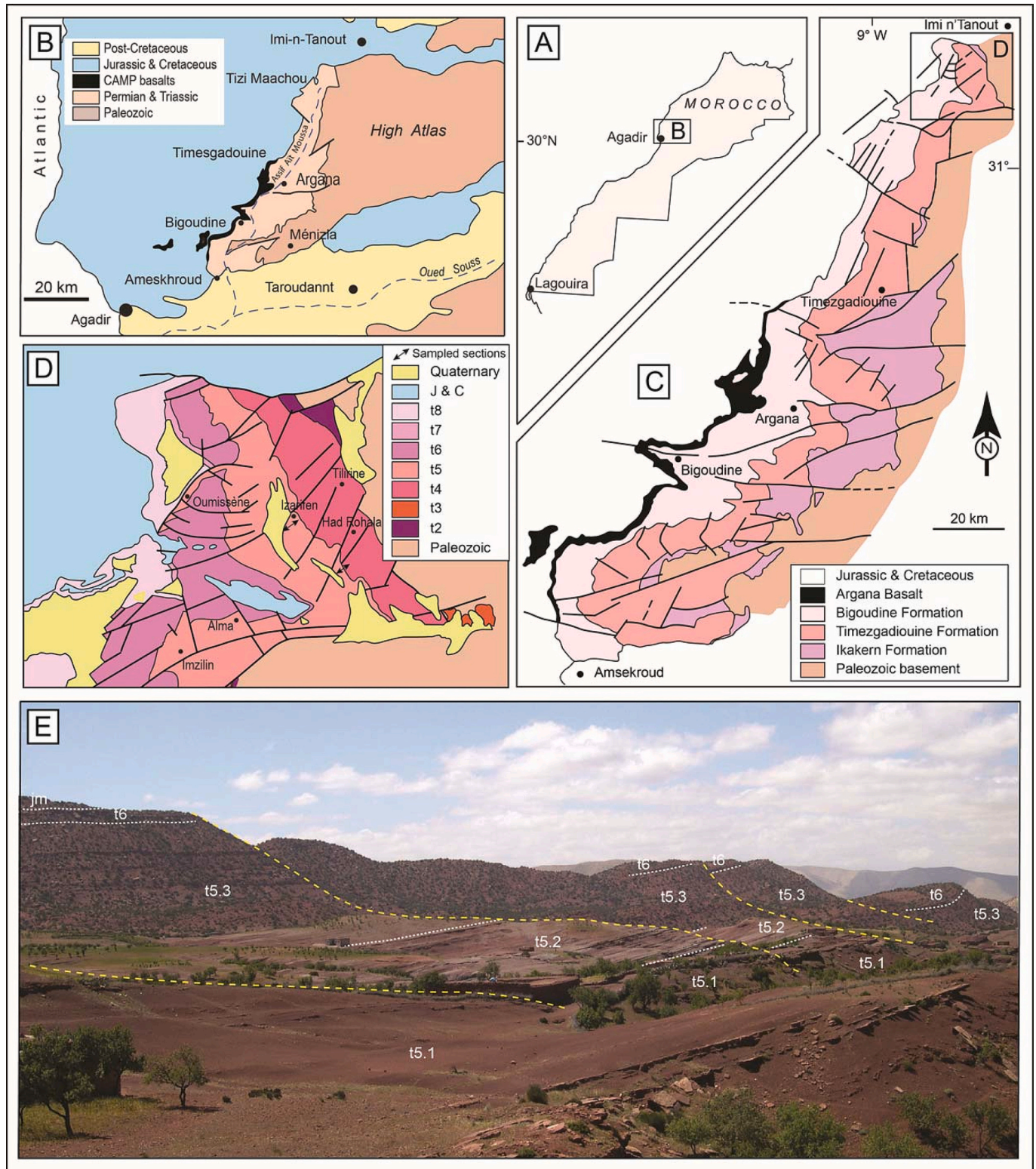


Fig. 1. Location and geological scheme of the study area. A-B: Position of the Argana Basin in Morocco; C: The Argana Basin, its main stratigraphical units and study area established in the northern part of the basin; D: Detail of the study area, and E: Field view of the study area.

approximately from 234 to 232 Ma, from the late Julian to early Tuvalian (Dal Corso et al., 2020). Precise age-determination is sometimes insufficient to differentiate this time interval when dealing with a continental sedimentary record. In fact, CPE studies have been less approached in continental basins until recent times, in which there has been a proliferation of works on the continental record worldwide. Many of these works have a multidisciplinary basis and combine studies of sedimentology, mineralogy, paleosols and paleontological information in a similar way to that presented in this work. (e.g., Barrenechea et al., 2018; Franz et al., 2019; Mancuso et al., 2020; Lu et al., 2021; Roghi et al., 2022). This area is, however, of special importance due to its Late Triassic equatorial closeness, but also because it shows very well exposed outcrops featuring a good palaeontological record (Zouheir et al., 2018, 2023 and references therein). Based on sedimentology, clay mineralogy and paleosol studies, this work focuses on the CPE in the continental Argana Basin, Western High Atlas, Morocco (Fig. 1 A-C). To identify the CPE time-interval, precise age data from clam shrimp (Crustacea-Branchiopoda-Diplostraca, formerly conchostracan and other names, see Gallego et al., 2020) associations in the Irohalene Member are here obtained for the first time. Previous studies based on tetrapod associations (e.g. Lucas, 2010; Lagnaoui et al., 2012, 2016; Zouheir et al., 2020) had already provided a late Ladinian-late Carnian age for the Irohalene Member. Although some studies have recently

related this member to the CPE (e.g., Mader et al., 2017) only the recent work of Zouheir et al. (2023) has focused the study of the Irohalene Member on this episode to date.

2. Geological setting

The Argana Basin is in the SW High Atlas, Morocco, and the study area was the northern part of this basin, about 55 km northeast of Agadir (Fig. 1, A-E). The basin is limited by two main faults, the Ichemraren-Imi N'Tanout and the El Menizla, to the north and south respectively. The latter fault occurs at the morphological boundary between the Souss plain and the Western High Atlas Mountains (Medina et al., 2000; Saber et al., 2001). The main sedimentary record consists of Permian, Triassic, and Early Jurassic red beds, trending NNE-SSW and parallel to the western border of the basin and unconformably resting on Paleozoic sediments (Brown, 1980; Hofmann et al., 2000; Saber et al., 2007). The Argana and neighboring basins were part of the rift system of the Central Atlantic Domain during the Triassic and have been described as conjugate basins of present-day Atlantic Canada (Manspeizer et al., 1978; Courel et al., 2003; Olsen et al., 2003; Whiteside et al., 2007; Redfern et al., 2010; Kent et al., 2017). As the result of reactivation of Variscan structures, the rift domain during the Carnian was increasingly extended with the development of half-grabens (Lavielle and Piqué, 1992). This

| Lower and Middle Jurassic post-rift succession | | | | | |
|--|---------------------------|------------------------------|--------------------------|--------------------------------|--------------------------------|
| Early Jurassic | Unknown Fm | t10- Supra-basaltic red beds | | Fluvial-Lacustrine | <i>Break-up Unconformity</i> |
| | | t9- Argana Basalt | | CAMP basalts | |
| Triassic | Bigoudine Fm | t8- Ait Hasseine Mudstone | | Fluvial-Lacustrine | <i>Syn-rift phase 2</i> |
| | | t7- Sidi Mansour Mudstone | | | |
| | | t6- Tadart Ouadou Sandstone | | Fluvial-Aeolian | |
| | Timezgadiouine Fm | t5- Irohalene Mudstone | t5.3 | Fluvial-Lacustrine | <i>Intra-rift Unconformity</i> |
| | | | t5.2 | | |
| t5.1 | | | | | |
| Timezgadiouine Fm | t4- Aglegal Sandstone | | Fluvial | <i>Syn-rift phase 1</i> | |
| | t3- Tanamert Conglomerate | | Alluvial | <i>Rift-onset Unconformity</i> | |
| | Permian | Ikakern Fm | t2- Tourbihine Sandstone | | Fluvial |
| t1- Driss River Conglomerate | | | Alluvial | <i>Pre-rift</i> | |
| Paleozoic basement | | | | | <i>Hercynian Unconformity</i> |

Fig. 2. Permian and Triassic lithostratigraphic units of the Argana Basin (based on Tixeront, 1973; Brown, 1980 and Hofmann et al., 2000). (For interpretation of the references to colour in this figure legend, the reader is referred to the web version of this article.)

extension was initiated by the reactivation of inherited faults and was marked by the presence of erosion truncation surfaces across the basin and an increase in distal alluvial and lacustrine facies (Leleu et al., 2016), as reflected in the Triassic stratigraphy of the Argana Basin.

The general Permian-Early Jurassic succession of the Argana Basin has been subdivided into 10 lithostratigraphic members denoted t1 to t10 (Tixeront, 1973; Brown, 1980; Hofmann et al., 2000) (Fig. 2), of which t1-t2 members are alluvial in origin and belong to the Ikkern Formation whose upper part provided the amphibian *Diplocaulus minimus*, which assign a Permian age to this formation. The Triassic succession appears in the Timezgadiouine (t3-t5) and the Bigoudine (t6-t8) formations. The whole Triassic sedimentary succession varies in thickness from 1300 m to 3500 m (Tixeront, 1973). The Tanamert conglomerate Member (t3), dated as Early Triassic by footprints (Tourani et al., 2000), is basically alluvial and rests unconformably on the t2, which represents the first Mesozoic pre-rift to syn-rift transition in the basin (Tourani et al., 2000). The Aglegal Sandstone Member (t4), dated as Middle Triassic based on vertebrate remains (Jalil et al., 2009) and tetrapod ichnofauna (Klein et al., 2011), is fluvial in origin and rests conformably on the unit t3 (Tixeront, 1973; Brown, 1980; Tourani et al., 2000). The Irohalene Mudstone Member (t5) rests conformably on t4 and is the focus of this study. The t5 unit appears as 200–500 m-thick alluvial-lacustrine mud-dominated succession, with intercalations of sandstone beds whose interconnectivity decreases upwards (Tourani et al., 2000; Hofmann et al., 2000; Zouheir et al., 2018, 2023). The Irohalene Member was assigned to the Carnian based on a tetrapod assemblage (Jalil, 1999; Lucas, 2010; Lagnaoui et al., 2012, 2016; Zouheir et al., 2020). Unconformably resting on t5, the Tadart Ouadou Sandstone Member (t6) represents the beginning of the second syn-rift phase in the basin (Tourani et al., 2000). The t6 unit is a succession of intercalated fluvial and eolian beds (Mader and Redfern, 2011). The middle and upper Bigoudine Formation is represented by t7, or Sidi Mansour mudstone, and t8, or Ait Hasseine mudstone, and both feature highly cyclical and laterally extensive playa deposits (Brown, 1980; Hofmann et al., 2000). The unit t9 is related to the Late Triassic – Early Jurassic CAMP flood basalts (Blackburn et al., 2013) and unit t10 appears as continental red beds overlying the basal flood basalts (Hofmann et al., 2000). The unit t10 is erosively overlain by the first Jurassic marine deposits (Daffaut et al., 1966; Harding and Brown, 1974; Duval-Arnould et al., 2021).

The excellent exposure of the Triassic members has allowed for detailed biostratigraphic studies in the Argana Basin (e.g., Jones, 1975; Dutuit, 1976, 1977a, 1977b; Tourani et al., 2000, 2010; Jalil and Peyer, 2007; Verati et al., 2007; Jalil et al., 2009; Lucas, 2010; Klein et al., 2010, 2011; Lagnaoui et al., 2012; Zouheir et al., 2018). These works provided an increasingly precise chronostratigraphy as well as correlations with neighboring basins such as the Essaouira Basin, some 100 km west of the study area (Mader et al., 2017).

3. Materials and methods

The stratigraphical sections Had Rohala and Izarifen (Fig. 1D) in the northern Argana Basin were selected for the study of the Irohalene Member (t5). This choice was based on the results of previous studies carried out in the area (e.g., Tourani et al., 2000; Hofmann et al., 2000). The two sections complement each other providing the complete record of the studied member. This study was based on detailed stratigraphic, sedimentologic, mineralogic and paleosol analyses. Chronostratigraphic information of the studied unit was obtained through a review of available paleontologic data and a detailed study of a clam shrimp association obtained in this work.

The clam shrimp study served to precise the age of the Irohalene Member of the Argana basin. It was carried out at the Laboratory of the Palaeontology and Palaeoenvironments of the Continental Phanerozoic Group at the Center for Applied Ecology of the Littoral (CECOAL-CONICET-UNNE, Argentina), by detailed studies of the stereoscopic

microscope photographs and SEM images of more than a hundred specimens from different levels. The collected samples are housed in the Department of Geology, Semlalia Faculty of Sciences, of the Cadi Ayyad University (Morocco) prefixed by CONCHO-t5. The photographs of the specimens were obtained by using Reflectance Transformation Imaging (RTI) at the Muséum National d'Histoire Naturelle (Paris) and were sent for their identification to CECOAL-CONICET-UNNE, Corrientes (Argentina). In this paper we follow the taxonomical and biostratigraphical schemes proposed by Kozur and Weems (2010), Scholze and Schneider (2015) and Geyer and Kelber (2017).

The sedimentological study was conducted in the field. Facies were differentiated following the nomenclature of Miall (1996, 2014) with minor modifications. Subsequently, the main associations of these facies were described as architectural elements to define the evolution of the sedimentary environment.

Our field study of paleosols followed the methodology proposed by Retallack, (1988, 2001). Paleosol levels were identified as pedotypes (Retallack, 1988) based on the presence of root traces, rhizoconcretions, soil horizons (e.g., A, Bt, Bk, C...) and soil structures (e.g. cracks, nodules, green mottling, types of peds...). Carbonate contents were assigned to the classes described by Machette (1985). Pedotypes were classified using the paleosol classification system of Mack et al. (1993) and the USDA Soil Taxonomy system (Soil Survey Staff, 1999).

For petrographic, mineralogic and geochemical studies, we sampled subsurface soil horizons of the most representative paleosols in the stratigraphic sections and other characteristic levels of lutite, carbonate, and hybrid oolitic sandstone of palustrine settings. Selected samples were powdered, dried, and sieved to 53 µm for homogenization, then dissolved by a combined acid attack employing, HNO₃, HClO₄, HF and HCl and prepared for standard whole rock analyses at the ALS Geochemistry facilities in Sevilla (Spain). For determination of major elements, Lithium Borate fusion decomposition of samples was followed by analysis through inductively-coupled plasma atomic emission spectroscopy (ICP-AES). Minor and trace elements were analyzed via an Inductively Coupled Plasma Mass Spectrometry (ICP-MS; LiBO₂ fusion) instrument following ALS ME-ICP06, ME-MS81, and ME-MS42 methods. Major-element, expressed as weight percentages of oxides (%), and minor-element and REE determinations, expressed as ppm, are provided as supplementary material (Table S1).

The chemical index of alteration (CIA) is a measure of the weathering of feldspar minerals and their hydration to form clay minerals. It was calculated from the equation proposed by Nesbitt and Young (1982) using molecular proportions: $CIA = [Al_2O_3 / (Al_2O_3 + CaO + Na_2O + K_2O)] \times 100$. Since potassium is susceptible to diagenetic alteration, Maynard (1992) proposed the CIA-K index: $CIA-K = [Al_2O_3 / (Al_2O_3 + CaO + Na_2O)] \times 100$. Sheldon et al. (2002) used a wide soil database and modern measurements of Mean Annual Precipitation (MAP; mm) to propose the equation $MAP = 14.265 (CIA-K) - 37.632$. The equation is useful in a precipitation range of 200–1600 mm/yr and offers an accuracy of $R^2 = 0.73$.

Paleosols and palustrine materials were mineralogically characterized by X-ray diffraction (XRD) analyses, including bulk mineralogy and clay mineral assemblages (Table S2). The samples were crushed into small pieces, ground in an agate mortar and then sieved to 53 µm. Analyses were carried out in a Bruker D8 Advance diffractometer (at the Faculty of Geology CAI, UCM) using Cu-K α radiation at 30 kV and 40 mA, a step size of 0.02 ($^{\circ}2\theta$), and a step time of 1 s, between 2 and 65 $^{\circ}2\theta$. Suspensions of the fraction <2 µm were obtained by sedimentation in distilled water, separating the upper 20 cm of the water column after 16 h of settling. From most of the samples, carbonate cements first had to be eliminated to obtain the suspension by treating the samples with sodium acetate and acetic acid, and repeated washings once the effervescence ceased, as recommended by Moore and Reynolds (1989). The clay fraction obtained was dried and 20 mg were weighed and mixed with 1 ml of distilled water in a test tube. The tube was placed in an ultrasound bath for 3 min to obtain a homogeneous suspension,

which was in turn poured from the test tube deposited on 2×2 cm glass slides to give a concentration of 5 mg/cm^2 in the aggregate. The aggregates were heat (TT) at 550°C for 2 h and solvated with ethylene glycol (EG) for at least 24 h to complete the characterization of the different clay minerals. The same scanning speed was used for the analysis, which was performed between 2 and $35^\circ 2\theta$. The software used

for the acquisition, treatment and evaluation of the data was DIF-FRACplus. A semi-quantitative analysis was also carried out using the Reference Intensity Ratio (RIR) method to obtain an estimate of relative variations in the different mineral phases.

To complete our detailed textural and compositional characterization of the samples, selected specimens were also subjected to scanning

| Previous records from other basins / authors | Biostratigraphic units / "Conchostracan" zones / substage age ranges (Kozur and Weems, 2010) | Proposed age of each taxa based on their records | Conchostracan recorded in the Argana Basin (This work) |
|--|---|--|---|
| <p>1) Germanic basin: Stuttgart Formation / Schilfsandstein -upper Grabfeld Formation.</p> <p>2) England: Dunscombe Mudstone, western England</p> <p>(Kozur and Weems, 2010; Geyer and Kelber, 2017).</p> | <p><i>Gregorisuella fimbriata</i>-<i>Laxitextella laxitexta</i> Zone / late Julian (formerly late Cordevolian)</p> | <p>late Julian – middle Tuvolian</p> | <p><i>Laxitextella laxitexta</i> Sandberger, 1871</p> |
| <p>1) Southern Germanic basin: Stuttgart Formation / Schilfsandstein – Estherias Beds – upper Grabfeld Formation</p> <p>(Geyer and Kelber, 2017).</p> | <p><i>Gregorisuella fimbriata</i>-<i>Laxitextella laxitexta</i> Zone / late Julian (formerly late Cordevolian)</p> | | |
| <p>1) Estheriensichten upper Grabfeld Formation, Germanic basin.</p> <p>2) Newark Supergroup: Irishtown Beds below New Oxford Formation, Gettysburg Basin (Maryland and Pennsylvania), USA.</p> <p>3) Falling Creek Formation, Taylorsville Basin (Virginia), USA.</p> <p>4) Tuckahoe Formation, Deep Run and Richmond basins (Virginia), USA.</p> <p>5) Lacustrine unit, Farmville, Briery Creek and Scottsburg basins (Virginia), USA.</p> <p>(Kozur and Weems, 2010).</p> | <p><i>Laxitextella multireticulata</i> Zone / early Julian (formerly early Cordevolian)</p> | <p>early Julian</p> | <p><i>Laxitextella multireticulata</i> Reible, 1962</p> |
| <p>1) Newark Supergroup USA: Lower fourth Lockatong Formation to Princeton Member, Lockatong Formation in the Newark Basin; Lower Cumnock Formation in the Sanford Subbasin</p> <p>(Kozur and Weems, 2010)</p> | <p><i>Howellisaura princetonensis</i> Zone / middle Tuvolian (equivalent to the <i>Laxitextella seegisi</i> Zone from the Germanic Basin)</p> | <p>middle Tuvolian</p> | <p>?<i>Howellisaura princetonensis</i> Bock, 1953</p> |
| <p>Germanic Basin, China, northeastern Canada, north Africa and Argentina</p> <p>(Kozur and Weems, 2010)</p> | <p><i>Euestheria minuta</i> Zone / Longobardian</p> | <p>Longobardian – early Julian</p> | <p>?<i>Euestheria minuta</i> von Zieten, 1833</p> |

Fig. 3. Main Triassic clam shrimps index species in the study area, their ages related to biostratigraphic units, and records.

electron microscopy (SEM). To this end, small fragments of the samples were dried in a stove at 50 °C for 48 h. The samples were glued onto a copper support and coated with gold. SEM analyses were carried out at the CAI of the Faculty of Geology of the UCM, using a JEOL JSM-820 microscope equipped with a microanalysis system and EDX Oxford ISIS-Link software for the acquisition, treatment, and assessment of data.

Samples for isotope analysis were mainly obtained from rhizoconcretions and carbonate nodules of paleosols. When paleosols lacked carbonate contents, we analyzed related palustrine layers of carbonate mudstones and oolitic hybrid sandstones (Table S3). Stable oxygen ($^{18}\text{O}/^{16}\text{O}$) and carbon ($^{13}\text{C}/^{12}\text{C}$) analyses were performed at the Stable Isotope Laboratory of the Institute of Geosciences IGEO (CSIC, UCM), Madrid, using an automated carbonate preparation device (Kiel-IV) coupled to a stable isotope ratio mass spectrometer (Thermo Scientific MAT 253). Values are reported in δ (‰) notation as $\delta^{18}\text{O}$ and $\delta^{13}\text{C}$ in relation to the Pee Dee Belemnite (PDB) standard. Typical analytical 1 σ errors were < 0.02 for $\delta^{18}\text{O}$ and < 0.01 for $\delta^{13}\text{C}$.

4. Age of the Irohalene Member

The age of the Irohalene Member of the Timezgadiouine Formation has been investigated since the 1970s. Until now, practically all these studies were based on diverse assemblages of tetrapod footprints (Lagnaoui et al., 2012, 2016; Zouheir et al., 2018, 2023), and vertebrate remains (Dutuit, 1976, 1977a, 1977b; Hunt and Lucas, 1991; Jalil, 1999; Jalil and Dutuit, 1996; Jalil and Peyer, 2007; Jalil et al., 2009; Lucas, 1998, 2010, 2018; Kammerer et al., 2011; Buffa et al., 2019). As discussed by Kammerer et al. (2011), all estimated ages broadly point to a Carnian or even late Carnian age for this member. In an interesting review by Mader et al. (2017), a more precise age, Julian - early Tuvlian, is provided based on a detailed review of previous works. The names of the Carnian substages here follow the nomenclature of Lucas (2010), and thus the Julian and Tuvlian represent the lower and upper Carnian respectively. As discussed by Krystyn (1978), the Cordevolian substage essentially refers to the same time interval as the Julian.

Several detailed biostratigraphic studies of the Permian and Triassic have been based on clam shrimp assemblages (e.g., Kozur, 1982; Kozur and Weems, 2010; Martens, 2012; Scholze and Schneider, 2015; Scholze et al., 2016, 2018; Schneider and Scholze, 2018). In Morocco, the first descriptions of Triassic clam shrimp were published by Defretin (1950) and Defretin and Fauvelet (1951), who mentioned the presence of *Euestheria minuta* von Zieten and *E. destombesi* Defretin species. Here, we describe the first clam shrimp association of the Irohalene Member in the Argana Basin (Fig. 3). The clam shrimp bearing interval was 82 m from the base in the Izarifen section and records an important association of clam shrimp characterized by *Laxitextella laxitexta* Sandberger, 1871, *Laxitextella multireticulata* Reible, 1962, *Laxitextella* sp., *Howellsaura princetonensis* Bock, 1953, *Euestheria minuta* von Zieten, 1833, *Euestheria* spp. and *Gregorisuella* sp. (Fig. 4). In the entire whole association identified in the study area, the most abundant species were the two firstly mentioned, *L. laxitexta* and *L. multireticulata* (Fig. 4A, B).

In biostratigraphic terms, the clam shrimp species here reported can be correlated with the *Gregorisuella fimbriata-Laxitextella laxitexta* Zone and *Laxitextella multireticulata* Zone of the Germanic Basin and Newark Supergroup (USA), as well as with the *Howellsaura princetonensis* Zone of the Newark Supergroup and, finally, with the *Euestheria minuta* Zone in China, northeastern Canada, North Africa and Argentina (Kozur and Weems, 2010). According to Kozur and Weems (2010), the *Gregorisuella fimbriata-Laxitextella laxitexta* Zone (accompanied by *Gregorisuella* and *Euestheria* species) was identified in the Germanic Basin and England indicating a middle Julian age, although they mention that the record of *L. laxitexta* reaches the late Julian and even the middle Tuvlian. Besides, Geyer and Kelber (2017) claimed that in the southern Germanic Basin this zone extends between the middle Julian - late Julian until the early Tuvlian. Moreover, the species *Laxitextella multireticulata* belongs to the biozone of the same name defined by Kozur and Weems (2010),

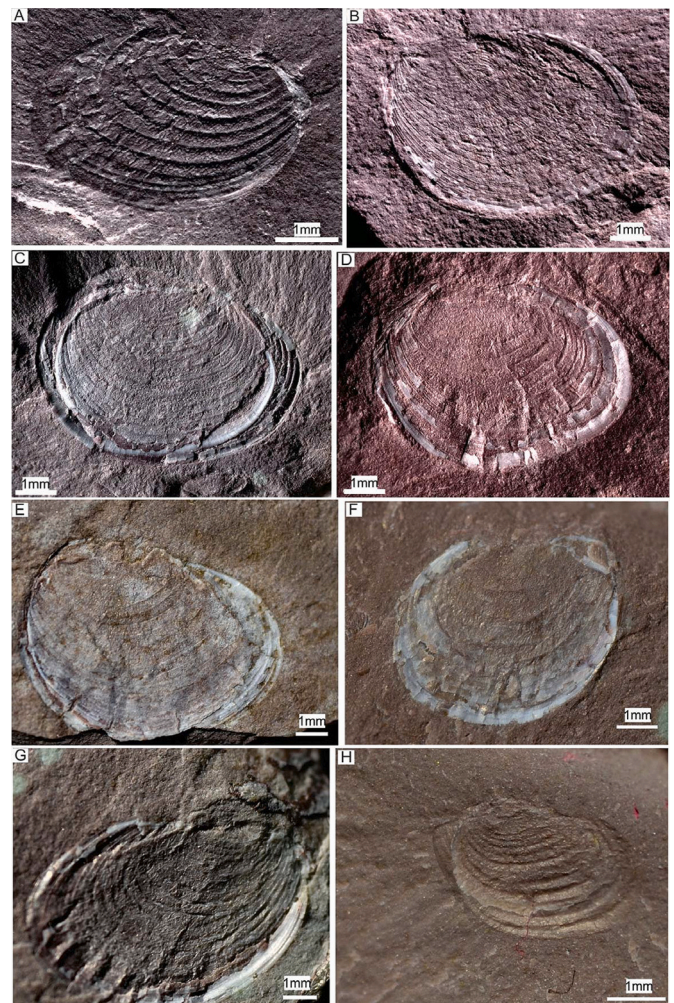


Fig. 4. Clam shrimps from the Irohalene Member: A) *Laxitextella laxitexta* Sandberger, 1871, B) *Laxitextella multireticulata* Reible, 1962, C–D) *Howellsaura princetonensis* Bock, 1953, E) *Euestheria minuta* von Zieten, 1833, F) *Euestheria* sp., G) *Gregorisuella* sp., H) *Shipingia* sp. Scale bar: 1 mm.

which indicates an early Julian age for the Germanic Basin and Newark Supergroup (USA). This zone is characterized by the presence of the species *Laxitextella multireticulata*, *Euestheria minuta* and *E. winterpockensis* (Bock). Kozur and Weems (2010) assigned the *Howellsaura princetonensis* Zone to the middle Tuvlian in the Newark Supergroup, which is equivalent to the *Laxitextella seegisi* Zone of the early to middle Tuvlian of the Germanic Basin. On the other hand, *Euestheria minuta* also occurs in the Germanic Basin, China, northeastern Canada, North Africa and Argentina. This taxon names the homonymous zone, together with *Lioleaia n. sp. A* (= *Praeleaia* sp. Warth, 1969) from the Longobardian (late Ladinian), that probably reaches the Julian in South America.

Gregorisuella could correspond to the previously mentioned *Gregorisuella fimbriata-Laxitextella laxitexta* Zone of middle Julian age and has been also related to *Gregorisuella bocki* (Olempska) from the *Laxitextella seegisi* Zone in the Germanic Basin, aged early to middle Tuvlian age. Finally, comparative studies of the clam shrimp levels in the Bocas Formation, Bucaramanga (Colombia) (Gallego et al., 2020) also helped us identify the presence in the association examined of *Laxitextella multireticulata* (Longobardian - Julian), *Shipingia hebaozhaiensis* Shen (in Zhang et al., 1976) (middle Norian), *Euestheria?* buravasi (early Norian) and *Wannerestheria* sp.

In summary, the clam shrimp assemblage of the Irohalene Member indicates a Carnian age, probably Julian to early Tuvlian age, therefore

coinciding with the CPE age-range recently detailed by Dal Corso et al. (2018). This more precise age fits well with the Carnian age provided by vertebrates for the Irohalene Member.

5. Depositional environment

The Irohalene Member crops out in the Argana Basin along the roughly N-S trending present-day depression which runs parallel to the southern extents of the High Atlas chain (Fig. 1). This member, which mainly comprises siltstones and mudstones with intercalated sandstones, varies widely in thickness possibly reaching 500 m (Mader et al., 2017). While Alpine tectonics caused significant deformation in the Central High Atlas, the Argana basin only experienced minor folding and the present-day dip of the Upper Triassic strata is $<30^\circ$ (Medina, 1995; Mader and Redfern, 2011). Our sedimentary study was based on a detailed description of the Had Rohala and Izarifen sections (Figs. 1D and 5). In the Had Roala section, only the lower 70 m of the Irohalene Member can be examined in detail. The Izarifen section reaches a thickness of 259 m but does not show the lowermost part of the member. Despite their thickness differences, these sections provide complementary sedimentary, pedogenetic and mineralogical data.

There are few previous detailed sedimentary studies of the Irohalene Member (t5) of the Timezgadouine Formation, and even fewer centering on the Had Rohala and Izarifen sections, as most studies on this member have mainly focused on tetrapods (e.g., Dutuit, 1977a, 1977b; Jalil and Peyer, 2007; Lucas, 2018; Zouheir et al., 2018). Among sedimentary studies on the Had Rohala and Izarifen or neighboring sections, the works of Brown (1980), Hofmann et al. (2000), and Baudon et al. (2012), Lagnaoui et al. (2012), Mader et al. (2017) and Zouheir et al. (2023) were avant-garde works, as they were the first to describe the detailed sedimentology of the Irohalene Member in the northern Argana basin. Some of them (e.g., Brown, 1980; Baudon et al., 2012) focused on the relationship between tectonics and sedimentation, while others (e.g., Lagnaoui et al., 2012; Mader et al., 2017; Zouheir et al., 2023) combined sedimentary studies with those of paleontological, mineralogical or paleosols characterization and evolution.

The present sedimentary study was based on identifying and interpreting 13 distinct facies (Table 1), 9 pedotypes (Table 2) and 10 main facies assemblages that constitute the architectural elements here defined, separated into those related to channels and those related to overbank and floodplains deposits (Figs. 6 and 7, respectively). The codes of facies and architectural elements are based on the nomenclature proposed by Miall (1996, 2014). These architectural elements were differentiated in the studied sections (Fig. 5) and represent the base of the interpretation of the sedimentary evolution of the Irohalene Member.

5.1. Architectural elements related to channels

In total, six facies make up four main facies assemblages in which the architectural elements CH, GB, LA and SB related to channel development can be differentiated (Fig. 6).

Architectural element CH. This element is mainly composed of fine to coarse-grained sandstones that may show isolated quartzite clasts, fine to coarse-grained sandstones constituting solitary or grouped trough cross-bedding stratification, and fine to medium-grained sandstones with current ripples, desiccation cracks, possible plant remains and bioturbation (Sp, St and Sr facies assemblage in Fig. 6). The vertical succession may show a fining or coarsening-upward tendency, is up to 4.3 m thick and frequently preserves lateral cutbank morphologies (Fig. 6a). This succession consists of a sand-dominated system represented by simple superimposed cross-bed sets which is overlain by thick floodplain sediments (element FF; Fig. 7). These bodies comprise vertically superimposed (ribbon) sandstone bodies. These channels tend to be isolated and bounded in most places by floodplain deposits that, in this case, contained development of paleosols. Their evolution may take

the form of crevassing in their upper part which commonly links neighboring channels (Fig. 6a). They could be related to a fixed channel of the anastomosed type, as the example described in the Cutler Group, New Mexico, by Ebert and Miall (1991).

Architectural element GB. This element is mainly comprised of clast supported crudely bedded gravel with horizontal bedding, and matrix-supported gravel with inverse to normal grading (Gh and Gmg facies assemblage in Fig. 6). Possibly reaching a thickness of 0.9 m of superimposed centimeter-thick beds, arranged according to irregular or diffuse contact between them, it consists of clast-supported and massive or crudely-bedded gravel (Fig. 6b). Facies are interpreted as inertial bedload or pseudoplastic sediments, under or near turbulent conditions that move during peak flows and grow upward and downstream via the addition of clasts during new episodes of high water and sediment discharge, as described in modern rivers by Bluck (1971) and Forbes (1983). Channels would be poorly developed during the deposition of architectural element GB, probably due to constant changes in discharge and sediment-transport patterns (De Haas et al., 2016).

Architectural element LA. This element is mainly comprised of fine to coarse-grained sandstones that may show isolated quartzite clasts, fine to coarse-grained sandstones constituting solitary or grouped trough cross-bedding stratification, fine to medium-grained sandstones with current ripples, desiccation cracks, possible plant remains and bioturbation, and fine to medium-grained sandstones with horizontal lamination (Sp, St, Sr and Sh facies assemblage in Fig. 6). It may reach a height of 3.5 m and length of 35 m and shows large-scale, gently dipping bounding surfaces (epsilon cross-bedding) related to successive pulses of lateral growth (Fig. 6d). The surfaces show offlapped upper termination that is followed by fine-grained facies related to the floodplain element (FF, Fig. 7). Decimeter- to centimeter-scale sand-mud alternations may form on the dipping surfaces. This element is interpreted as lateral-accretion deposits related to a meandering sandy fluvial system, similar to the examples described by Puigdefábregas and van Vliet (1978) in the Cenozoic of the Southern Spanish Pyrenees, in the Late Cretaceous Mancos Formation (USA) by Wu et al. (2016), and in the Permian Clear Fork Formation (USA) by Simon and Gibling (2017). Sand-mud alternations could reflect varying transport energies (Wood, 1989).

Architectural element SB. This element is mainly composed of fine to coarse-grained sandstones constituting solitary or grouped trough cross-bedding stratification, fine to coarse-grained sandstones that may show isolated quartzite clasts, fine to medium-grained sandstones with horizontal lamination, and fine to medium-grained sandstones with current ripples, desiccation cracks, possible plant remains and bioturbation (St, Sp, Sh and Sr facies assemblage in Fig. 6). It is represented by 0.3–0.5 m thick beds of medium to fine-grain sandstones with planar and trough cross-stratification (Fig. 6c). The vertical succession shows a fining-upward tendency and, when complete, it features current ripples and horizontal lamination at the top. The base is lightly erosive. These beds may appear isolated or two or three of them stacked, but they always develop into floodplain facies (element FF). These sets of beds can comprise channel belt morphologies directly overlying floodplain fines. They are interpreted as sand bed forms that represent minor bars related to crevasse deposits, as the examples described by Burns et al. (2017) in the Cretaceous Neslen Formation, Utah (USA), and Gulliford et al. (2017) in the Beaufort Group, South Africa. The vertical accumulation of beds may reflect aggradation and reduction in water depth, as described in the Carboniferous of the Pocahontas Basin by Horne and Fern (1976).

5.2. Architectural elements related to overbank and floodplains

A total of thirteen facies make up six main facies assemblages that serve to differentiate CS, CR, FF, FFch, LCs and LCc architectural elements which are related to floodplains and overbank deposits (Fig. 7). The paleosols associated with floodplain deposits will be described in another chapter.

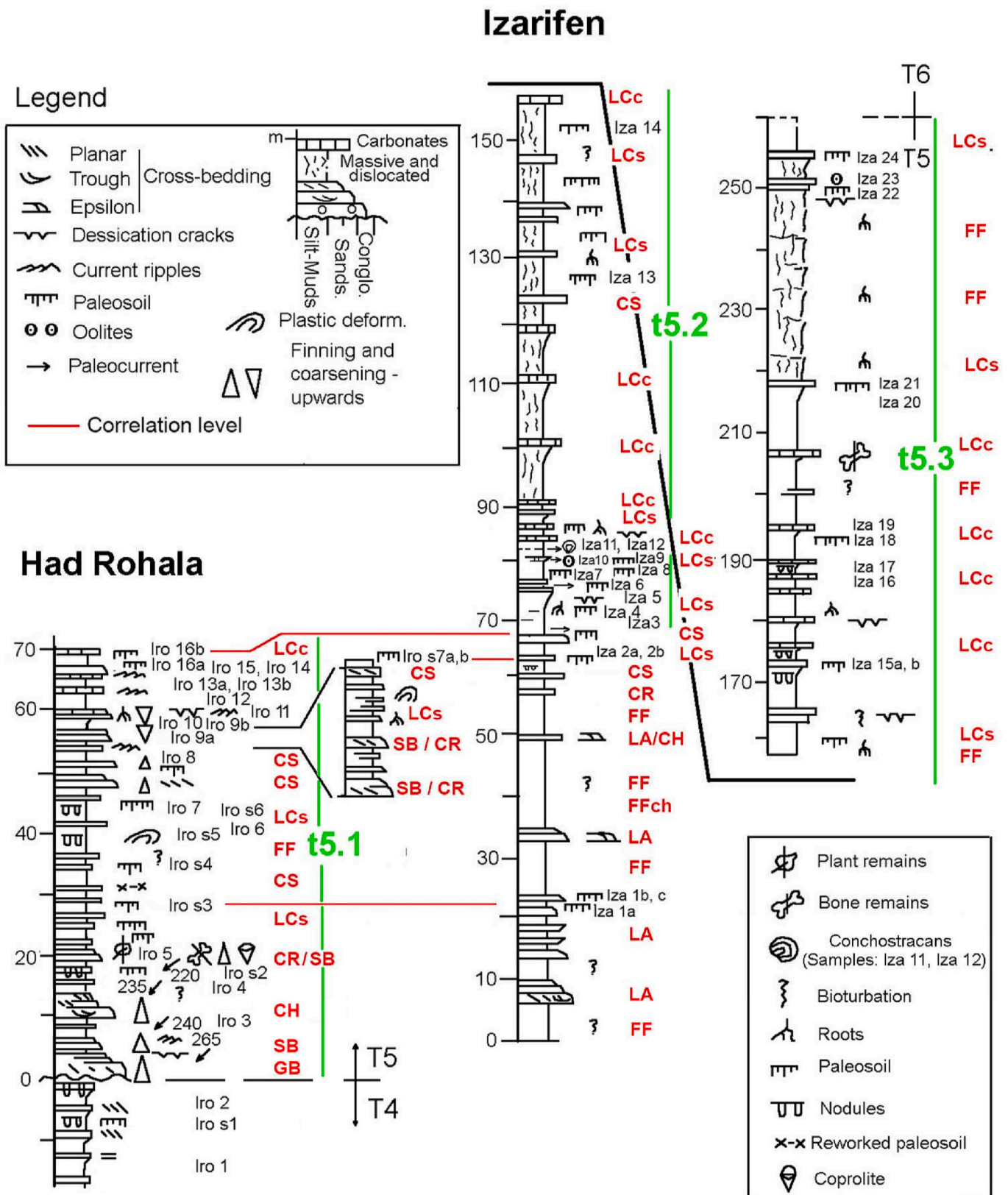


Fig. 5. Had Rohala and Izarifien sections (see Fig. 1 for their locations in the area of the Argana Basin examined). The samples analyzed are indicated in both sections. See Figs. 6 and 7 for a description of the architectural elements.

Table 1

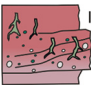
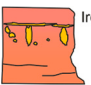
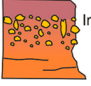


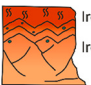
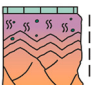
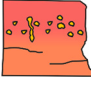
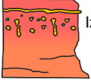
Facies distinguished in the Irohalene Member. See Figs. 5 and 6 for their composition as defined architectural elements. Facies are mainly based on Miall's classification system (Miall, 1996, 2014).

| Facies |
|---|
| Gmg: Matrix-supported gravel with inverse to normal grading. |
| Gh: Clast supported crudely bedded gravel with horizontal bedding. |
| Sp: Fine to coarse-grained sandstones (may show isolated quartzite clasts) constituting solitary or grouped planar cross-bedding stratification. |
| St: Fine to coarse-grained sandstones constituting solitary or grouped trough cross-bedding stratification. |
| Sh: Fine to medium-grained sandstones with horizontal lamination. |
| Sr: Fine to medium-grained sandstones with current ripples, desiccation cracks, possible plant remains and bioturbation. |
| Sl: Fine to coarse-grained sandstones with low angle (<15°) cross-beds. |
| Fm: Massive mud or silt with desiccation cracks. |
| Fsm: Massive silt or mud. |
| Fr: Massive mud or silt with roots and bioturbation. |
| Fl: Fine-grained sandstones, mud or silt with fine lamination and small ripples. |
| Fs: Massive mudstones with paleosols. |
| C: Carbonaceous mud and/or millimetre thick beds of limestones / dolomites. |
| P: Paleosols with possible carbonate nodules development. |

Architectural element CS. This element is mainly comprised of fine to coarse-grained sandstones constituting solitary or grouped trough cross-bedding stratification, fine to coarse-grained sandstones that may show

Table 2

Pedotypes distinguished (P1 to P9) and their field diagnoses, main geochemical and mineralogical characteristics, and inferred classification. Q (Quartz), Il (Illite), Cc (Calcite), Dol (Dolomite), Hem (Hematite), Ab (Albite), Sm (Smectite), Chl (Chlorite), Anl (Analcime).

| Pedotype | Field diagnosis | Mineralogical and geochemical features | Mack et al. (1993) | U.S. Taxonomy (Soil Survey Staff, 1999) |
|--|---|--|--------------------|---|
| P1  Iro-1 | Drab haloed root traces and green mottling. Weakly developed mainly on conglomerate and coarse-grained sandstone. A–C horizons. | Moderate leaching of A horizon (Ba/Sr > 3). Well-drained (low values of Alkalies/Alumina). Mineralogy dominated by Q and Il, minor Cc, Hem, Ab. Significant contents of Sme but low Chl quantities. No Anl. | Gleyed Protosol | Entisol (Aquent) |
| P2  Iro-2 | Platy cementation on top of Bk. Thick and sparse rhizoconcretions. Disperse carbonate nodules at stage II (Machette, 1985). Bk–C horizons. | Mineralogy of silty-clayey materials are dominated by Q and Il, with minor Hem, Ab and Anl, traces of Cc and/or Dol. No Sme detected. | Calcisol | Aridisol (Haplocalcid) |
| P3  Iro-s2 | Carbonate nodules and rhizoconcretions at stage II-III under a red Argillic Bt horizon with few slickenside structures. Bt-Bk-C horizons. | Nodules of dolomitic composition. High contents of Sr and Ba. Mineralogical assemblage composed by Q, Il, minor Hem, Ab and Anl, Cc and Dol. No Sme recognized. | Argillic Calcisol | Aridisol (Calciargid) |
| P4  Iza-1c, Iro-s3, Iza-1a, Iza-1b, Iro-6 | Natric horizon with convex surface and domed columnar ped structures. Dehydration cracks. Clay illuviation. Btn1-Btn2-Cn horizons. | High Na ₂ O content in clayey material. In the columnar horizon Na ⁺ and K ⁺ are lost by illuviation and only columnar soil structure remains as a sign of a natric horizon. Mineralogy dominated by Q and Il, minor Cc, Hem, Ab and the highest contents of Anl. Chl present in the clay fraction, but no Sm detected. | Natric Argillisol | Aridisol (Natrargid) |
| P5  Iro-8, Iro-7, Iro-s6, Iro-s5, Iro-s4 | Long rhizoconcretions and thick nodules on clayey material with ferric pedogenic ooids. Bk horizon at stage III. B-Bks-C horizons. | Dolomitic composition. Very low Hydrolysis (highest Bases/Al). High values of MgO and Sc. Mineralogical assemblage dominated by Q and Il, minor Cc, Hem, Ab and Anl. Significant Chl values. No Sme. | Ferric Calcisol | Aridisol (Haplocalcid) |
| P6  Iro-7a, Iro-7b | Profuse pedoturbation. Red B horizon. Gilgai structures, slickensides, desiccation cracks, green mottling. B-Bss-C horizons. | Low values of Mg, Sr, and Bases/Al ratios. High CIA-K index. Mineralogy characterized by Q and Il, Minor Ab, Hem and Anl. Presence of Chl and significant Sme contents. | Vertisol | Vertisol (Aquent) |
| P7  Iza-2a, Iro-16a, Iza-2b, Iro-16b | Intense pedoturbation. Purple B horizon. Gilgai structures. Slickensides, root traces, clastic dikes, and green mottling. Related with palustrine carbonates. Bw-Bssg-C horizons. | Intense leaching in upper horizons (high Ba/Sr and low Bases/Al ratios). Mineralogy defined by Q and minor Cc, Dol, Hem, Ab and Anl. Il and Chl recognized. Samples with the highest Sme contents. | Gleyed Vertisol | Vertisol (Epiquent) |
| P8  Iza-16,17, Iza-15a,b | Small carbonate nodules and veinlets 15 cm deep at stage I on red siltstones. Bk–C horizons | Increases in Mg, Ca, Sr, and Bases/Al ratios. Mineralogical assemblage defined by Q and minor Cc, Dol, Hem, Ab and Anl. Clay fraction dominated by Il, lower Sme contents and significant presence of Chl. | Calcic Protosol | Inceptisol |
| P9  Iza-24 | Red mudstones with thin petrocalcic horizon, nodules, rhizoconcretions and cracks. Green Mottling around root traces. K-Bk-C. | Similar contents of Mg, Ca, Sr, and Bases/Al ratios as P8. Mineralogy defined by Q and minor Cc, Hem, Ab and Anl. Clay fraction dominated by Il and Sme. No Chl recognized. Significant contents of Dol. | Calcisol | Aridisol (Petrocalcic) |

isolated quartzite clasts, fine to medium-grained sandstones with horizontal lamination, fine to coarse-grained sandstones with low angle cross-beds, and fine-grained sandstones, mud or silt with fine lamination and small ripples (St, Sp, Sh, Sl and Fl facies assemblage in Fig. 7). It is represented by 0.8–1.4 m thick tabular, flat-based beds of fine to medium sandstone with common interbedded fine sediments (Fig. 6a). This element reaches a lateral extension of >100 m and can be stacked or separated by thin beds of fines, which laterally passes to thick floodplain deposits (element FF). The sandstone beds display low-angle accretion surfaces and may show a coarsening or fining-upward arrangement. This element has been interpreted as crevasse splay deposits such as the examples described by Bridge and Demicco (2008) in the lower Permian of Nova Scotia, and by Simon and Gibling (2017) in the Permian Clear Fork Formation (USA).

Architectural element CR. This element consists mainly of fine to coarse-grained sandstones constituting solitary or grouped trough cross-bedding stratification, fine to medium-grained sandstones with horizontal lamination, fine to coarse-grained sandstones that may show isolated quartzite clasts, and fine to medium-grained sandstones with current ripples, desiccation cracks, possible plant remains and bioturbation (St, Sl, Sh and Sr facies assemblage in Fig. 7). It shows a vertical ribbon pattern of medium-grained sands appearing as 0.5–1.3 m thick beds. Ribbons may be tens of meters wide and up to 3.5 m thick (Fig. 6b). Individual beds show a planar base but the general stacked

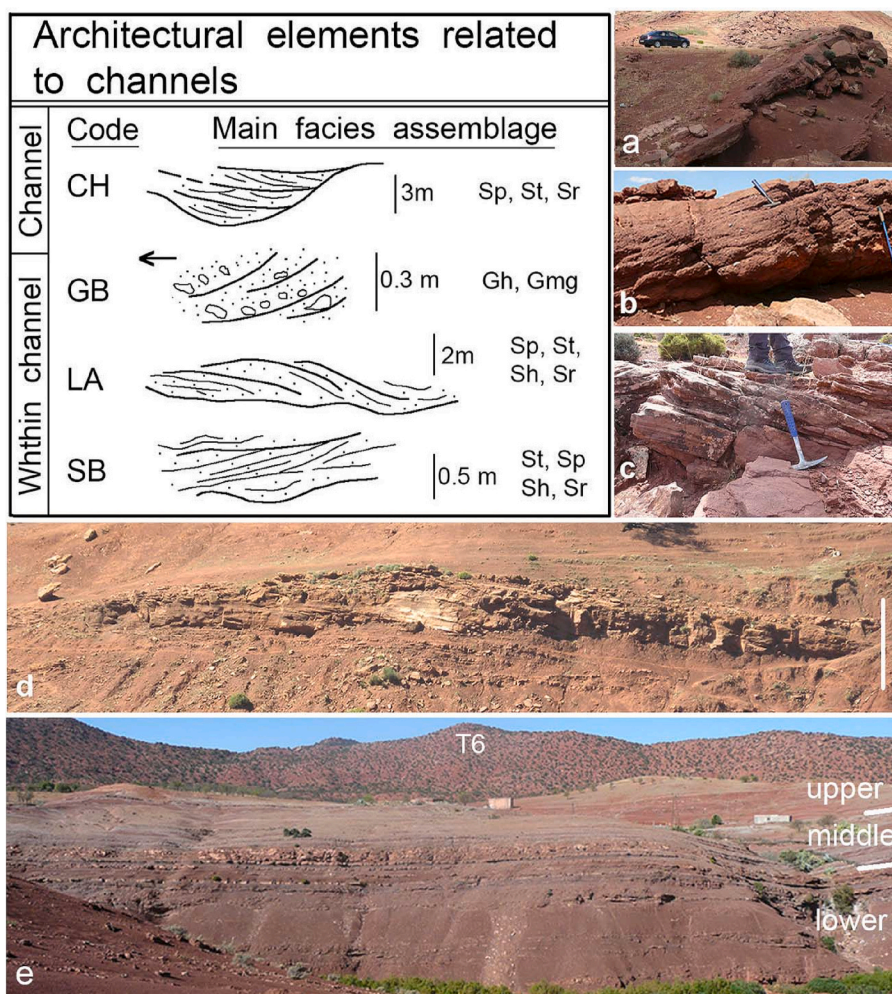


Fig. 6. Architectural elements (AE) related to channels and their main facies assemblages: a- CH, b- GB, c- SB, d- LA; e- general view of the Irohalene Member in the Izarifen section. See [Table 1](#) for facies codes.

morphology reveals a concave erosive base on the floodplain deposits. The element is interpreted as crevasse channel deposits, similar to the example described by [Smith et al. \(1989\)](#) for the Saskatchewan River. [Ebert and Miall \(1991\)](#) described examples of erosive and concave bases (“U-shaped” morphology) in crevasse splay deposits in the Permian Cutler Formation, New Mexico (USA).

Architectural element FF. This element consists mainly of massive mud or silt with roots and bioturbation, fine to medium-grained sandstones with current ripples, desiccation cracks, possible plant remains and bioturbation, and Paleosoils with possible carbonate nodules development (Fr, Sr and P facies assemblage in [Fig. 7](#)). This element is mostly represented by sheet-like units tens of meters thick of red mudstones and siltstones with thin intercalated fine to medium-grained sand beds and paleosol developments that may show carbonate nodules ([Fig. 7 c](#)), as will be described in the next chapter. Laterally, this element may extend across hundreds of meters. Fine sediments tend to be massive and disrupted by organic activity, while sandstones commonly show ripple cross-lamination, bioturbation by roots, and burrows and desiccation cracks. It is interpreted as floodplain fines, as the examples described by [Foix et al. \(2013\)](#) in the Cenozoic Río Chico Formation, Argentina, where good examples of intercalated fine-grain sand bodies into the floodplain fines were described. Evidence of desiccation and pedogenesis processes has been related to seasonal or longer-term drying out of the floodplain ([Willis and Behrensmeier, 1994](#); [Ghazy and Mountney, 2009](#)).

Architectural element FFch. This element consists mainly of massive

mud or silt with desiccation cracks, fine-grained sandstones, mud or silt with fine lamination and small ripples, massive mud or silt with roots and bioturbation, massive silt or mud, and massive mudstones with paleosoils (Fm, Fl, Fr, Fsm and Fs facies assemblage in [Fig. 7](#)). It is represented by siltstone and fine to medium-grained sands and has a ribbon near “U-shaped” morphology of up to 1.7 m thick and <3 m wide. The lateral limits, or cut-bank, are diffuse, as this element is surrounded by floodplain fines that are similar in colour and lithology ([Fig. 7 d](#)). The element is interpreted as an abandoned channel. In some cases, it is related to the lateral development of an LA element, thus indicating an abandoned channel related to the development dynamics of a meandering fluvial system, similar to the cases described in the Mississippi river system by [Farrell \(1987\)](#) resulting from chute or neck cut off processes.

Architectural elements LCs and LCc. These elements mainly comprise massive mud or silt with desiccation cracks, fine-grained sandstones, mud or silt with fine lamination and small ripples, massive mud or silt with roots and bioturbation, massive silt or mud, paleosoils with possible carbonate nodules development, carbonaceous and/or millimetre thick beds of limestones or dolomites (Fm, Fl, Fr, Fsm, P, C, and Sr facies assemblages in [Fig. 7](#)). They are represented by a 0.6–1.2 m thick succession with a thickening-upward tendency. They contain massive mudstones – siltstones beds in their lower part, and fine-grained sands in the upper portion that may feature ripple cross-lamination, desiccation cracks and bioturbation by roots and burrows at the top. Colors range from red to purple. Architectural element LCc shows a high carbonate

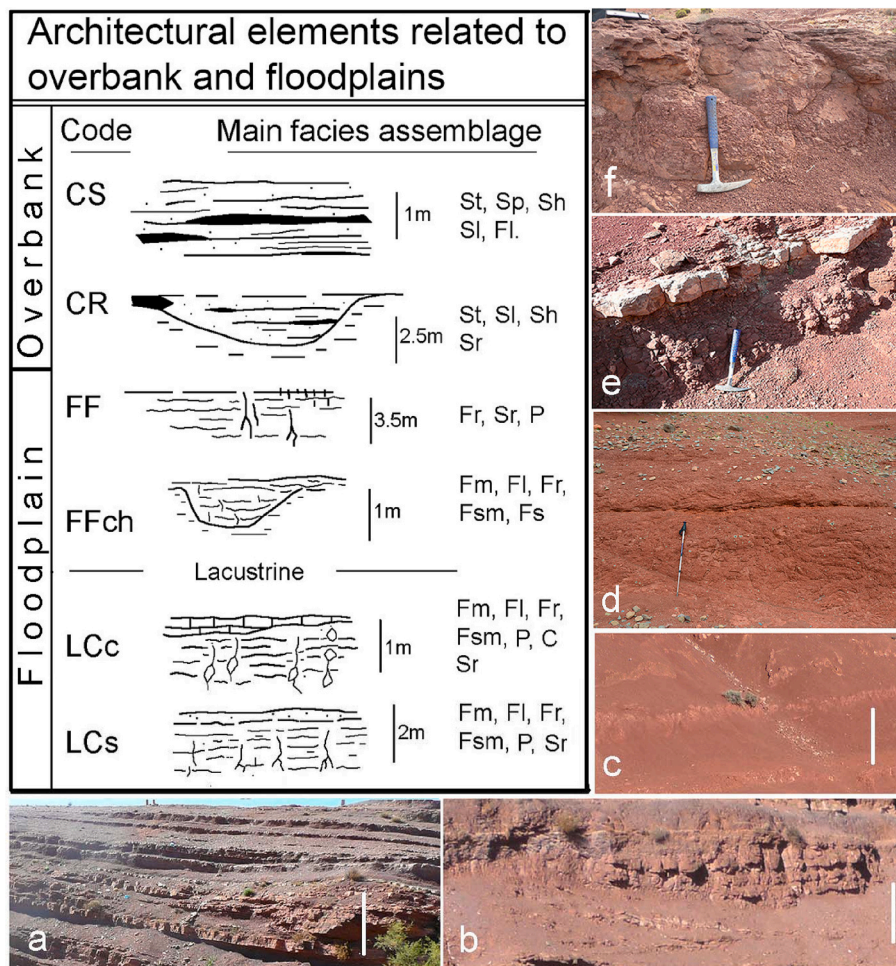


Fig. 7. Architectural elements (AE) related to floodplain and overbank deposits and their main facies assemblages: a- CS, b- CR, c- FF, d- FFch, e- LCs, f- LCc. See Table 1 for facies codes.

content at the top that may take the form of millimetre to centimeter-thick limestone-dolomite beds (Fig. 7e). This latter element may also show the development of carbonate nodules in its lower and middle muddy-silty parts, while roots remains are common in element LCs (Fig. 7f). These carbonate and siliciclastic beds may contain oolites, fish remains and brachiopods (clam shrimps). LCc and LCs are interpreted respectively as carbonate and siliciclastic ponds or lakes. Similar examples have been described in Permian rocks by Ghazy and Mountney (2009), and Michel et al. (2015) and Mercuzot et al. (2022).

6. Paleosols description and classification

In the Timezgadiouime Formation, nine pedotypes were differentiated: P1 for the t4 Aglegal Sandstone Member and P2 to P9 for the t5 Irohalene Mudstone Member. Field diagnoses, main mineralogic and inferred classification are summarized in Table 2. Field diagnosis and mineralogy were complemented with geochemical data from paleosol samples and related levels such as palustrine materials. The geochemical results and the most common weathering indices are presented in Table S1 of the supplementary material. Interpreted field and thin-section photographs of selected profiles are provided in Figs. 8 and 9.

Pedotype P1 displayed a poor horizonation and appeared weakly developed on the coarse-grained materials of the t4 Aglegal Sandstone Member. This pedotype showed hydromorphic features such as drab haloed root traces and common green mottles. Its Ba/Sr index around 3 and low values of $(K + Na)/Al$ are indicative of good drainage (Table S1; Sheldon and Tabor, 2009; Retallack, 2001). As its poorly developed

profiles are subdivided into horizons A–C with abundant gley features, P1 was classified as a Gleyed Protosol (Table 2).

The first paleosols of the t5 Irohalene Mudstone Member were assigned to pedotype P2. These were characterized by a Bk horizon at stage II of carbonate accumulation (Machette, 1985), and by thick yellow rhizoconcretions (Fig. 8A). In some profiles, a thin and sub-horizontal accumulation of carbonate appeared at the top of the Bk horizon. The mineralogy of its fine-grained materials was dominated by quartz and illite. Smectite was not recognized. Pedotype P2 has been classified as a Calcisol (Mack et al., 1993). Again, a Bk of carbonate accumulation at stage II-III characterizes pedotype P3, but its profiles also showed a subsurface horizon of clay accumulation (Bt) on top of the Bk horizon (Fig. 8B). High MgO contents were observed in the calcic nodular horizon, which also featured very high Sr and Ba levels (Table S1). No smectite has been found in its mineralogical assemblage (Table S2).

Some of the features observed in P1, P2, and P3 pedotypes, such as green to gray rhizohaloes, green reduction spots, and calcareous rhizoconcretions, were documented by Zouheir et al. (2023) in the lower part of the Irohalene Member. These authors suggested the interaction of plants in environments with fluctuations in the water table, humidity and drainage.

The most characteristic feature of pedotype P4 was its indurated horizon bearing domed columnar ped structures and desiccation polygons (Fig. 8C, D). Faces of columnar peds were in many cases rounded by cracks filled with clays. Features of clay illuviation have been also observed in thin sections. Based on the illuvial accumulation of clays and

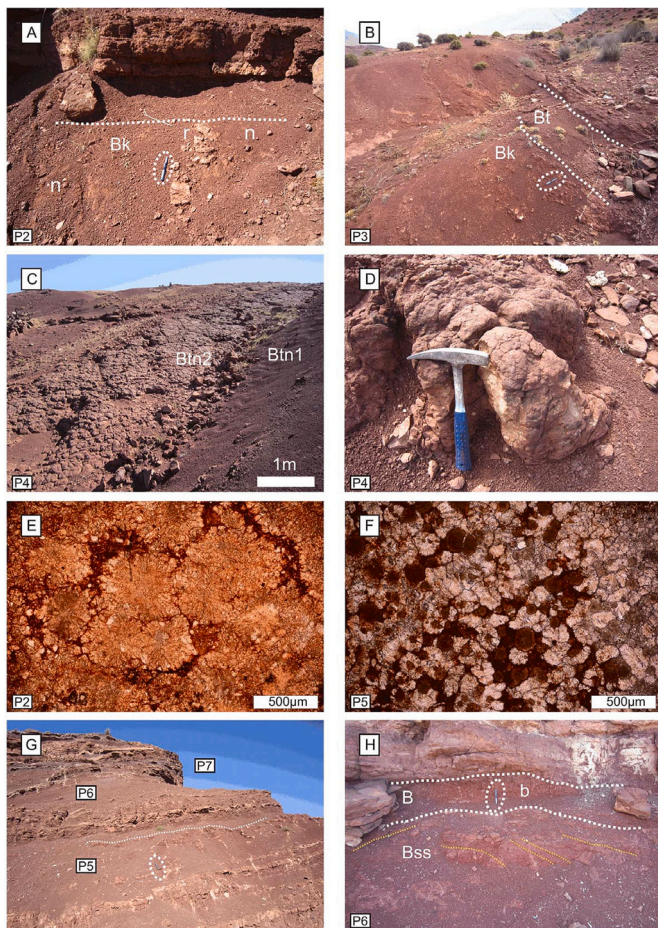


Fig. 8. A) Thick rhizoconcretion (r) and carbonate nodules (n) found in the fine-grained Bk horizon of pedotype P2. B) Subsurface accumulation of clays in the Bt horizon of pedotype P3. C) Field picture of the indurated natric horizon (Btn2) of pedotype P4 seen from above. Note the columnar pattern with rounded tops. D) Close-up view of the natric horizon of P4. E) Photomicrograph taken under plane-polarized light of a carbonate nodule in the Bk horizon of P2. Coarse spar replaces the clayey material in a radial pattern (sample Iro-2). F) Earlier ferric pedogenic ooids in the matrix were affected by a coarse spar growing in the Bk horizon of P5 (sample Iro-s6). G) Long rhizoconcretions and carbonate accumulation in the Bk horizon of P5. Up in the section, a P6 profile can be observed, along with purple subsurface horizons characterizing the presence of P7. H) Incomplete intersecting slickensides structures in the Bss horizon under the clayey B horizon with some bioturbation (b) of P6. Pen (14 cm) and hammer (35 cm) outlined with a white dashed line for scale. (For interpretation of the references to colour in this figure legend, the reader is referred to the web version of this article.)

its columnar structure, this indurated layer has been described as a natric horizon (Soil Survey Staff, 1999). Although a natric horizon must have an exchangeable-sodium saturation of over 15%, low Na_2O values below 3.53% were obtained from the horizons of pedotype P4 (Table S2). In similar paleosols, Na^+ and K^+ were mostly lost from the columnar horizon by illuviation, and only a columnar soil structure and values of 8–12% MgO and 13–20% CaO persisted as indicators of a natric horizon (McCahon and Miller, 1997; Soil Survey Staff, 1999). The presence of sodium was also indicated by XRD analyses through a higher content of analcime, a hydrated sodium aluminum silicate (Table S1). Pedotype P4 was classified as a Natric Argillisol (Table 2).

Pedotype P5 was characterized by a Bk horizon at stage III with thick nodules and long rhizoconcretions (Fig. 8G). In thin sections, coarse subeuhedral carbonate replaced the original clayey sediment with ferric pedogenic ooids (Fig. 8F). Pedotype P5 returned high values of MgO and Sc, and the highest Bases/Al index, which is indicative of low hydrolysis

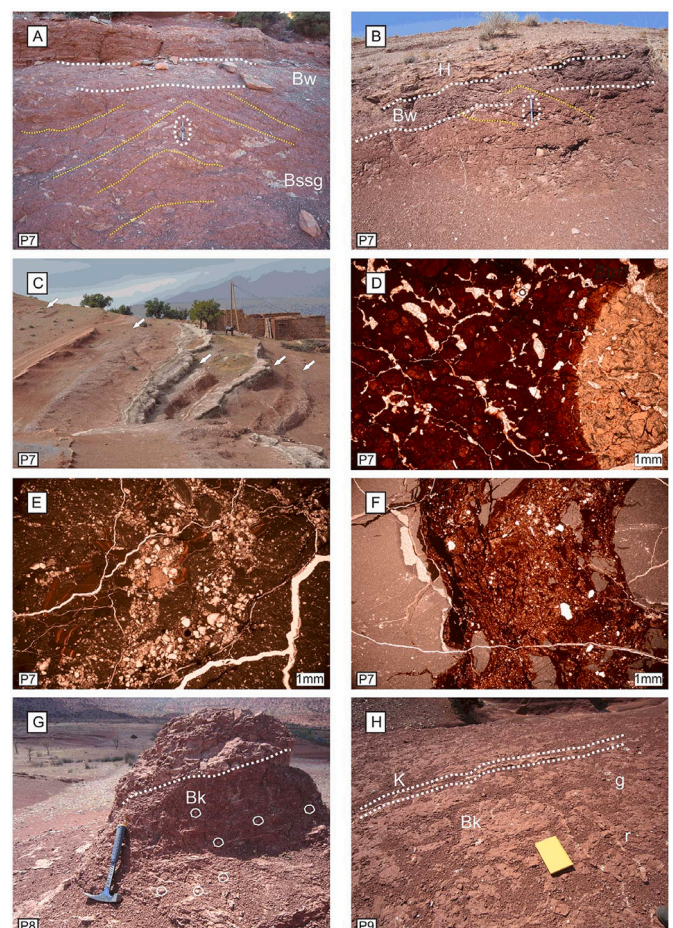


Fig. 9. A) Intersected slickensides producing a wedge-shaped structure in the Bssg horizon of P7. Swelling-shrinking processes produce a landscape of mounds and depressions called a Gilgai microtopography. A purple Bw horizon and dispersed green mottling can also be observed. B) Colored Bw horizon of P7 capped by fine-grained and oolitic hybrid sandstones (H). C) Purple Bw horizons of P7 (white arrows) intercalated with carbonate levels and palustrine materials. D) Fine subangular blocky structure with fine vesicular pores in the Bssg horizon of a P7. Note the gray depletion redox area seen on the right of the picture (sample Iza-20). E) Palustrine materials on top of P7 (sample Iza-12). Blocky angular structure with a heterogeneous groundmass composed of clay aggregates, sandy material, and oolites. F) Upper part of the Bw horizon of P7. Desiccation cracks in gray clay are filled with red silty materials (sample Iro-14). G) Calcite nodules in stage II Bk horizon of P8. H) P9 profile showing a thin petrocalcic horizon (K) on top of a Bk horizon featuring long rhizoconcretions (r) and green mottling (g). Pen (14 cm) and hammer (35 cm) provided for scale. (For interpretation of the references to colour in this figure legend, the reader is referred to the web version of this article.)

(Sheldon and Tabor, 2009). In its mineralogical assemblage, there was a significant amount of chlorite but smectite was not detected. According to the presence of iron oxides, this pedotype was classified as a Ferric Calcisol (Table 2).

Pedotype P6 was characterized by a reduction in MgO and Bases to Alumina values, along with a pronounced increase in smectite. This pedotype shows a B horizon with intersected slickensides that generate a wedge-shaped structure (Fig. 8H). Other common features were desiccation cracks, green mottling, and abundant vertical bioturbation. Repeated hummock and swale structures are also known as Gilgai microrelief, formed by shrink-swell processes in expanding clay soils (Retallack, 2001). Smectite clays feature a high shrink-swell capacity and Gilgai structures are commonly observed in Vertisols in climates showing distinct wet and dry seasons (Mack et al., 1993; Retallack,

2001; Schulze, 2005).

The samples of pedotype P7 showed the highest smectite contents and evident Gilgai structures (Fig. 9A). These structures occurred under a Bw horizon with purple colour that is commonly associated with layers of carbonate, greenish lutites, and hybrid oolitic sandstone from palustrine environments (Fig. 9B, C). Palustrine materials and the upper part of P7 display conspicuous desiccation cracks. In thin sections, the lower homogeneous clayey red horizon with slickensides has a fine subangular blocky structure with some green mottling and microvoids (Fig. 9D). This, contrasts with the gray and greenish colors of the upper horizons showing bioturbation, cracks, and a heterogeneous material composed of lutitic intraclasts, clay coatings, sand-sized particles, and oolites (Fig. 9E, F). Intense leaching is interpreted from the first profiles of pedotype P7, which have high Ba/Sr and low Bases/Al ratios (Table S1). However, the upper profiles in the section were characterized by more intense purple and blue colors (Fig. 9C) and by limited leaching, probably related to slow permeability of the smectite-dominated profiles (18 to 31%) and prolonged periods of waterlogging. Pedotype P7 was classified as a Gleyed Vertisol (Table 2). Likewise, some of the features observed in P6 and P7 pedotypes, such as pseudo-anticlines, pedogenic slickensides, and root traces were associated by Zouheir et al. (2023) with red to purple Vertisols.

Blue and purple colors were not observed in pedotype P8, a poorly developed paleosol classified as a Calcic Protosol, with small carbonate nodules at stage I on red siltstones (Fig. 9G), and increases in MgO, CaO, Sr, and Bases/Al values (Table S1). Lower smectite contents (11 to 12%) were observed in the clay fraction, which was dominated by illite and chlorite.

Found at the top of t5.3, close to the boundary with the Bigoudine Formation., pedotype P9 was defined as a Calcisol according to the classification system of Mack et al. (1993), yet its carbonate accumulation in a thin petrocalcic horizon on top of a red clayey horizon with disperse carbonate nodules and rhizoconcretions (Fig. 9H) allows its assignment to the Petrocalcids great group (Soil Survey Staff, 1999).

7. Carbon and oxygen stable isotope data

Carbon stable isotope values ($\delta^{13}\text{C}$) of soil-formed carbonates mainly depend on the composition of land plants, but also on the composition of soil waters and soil dissolved atmospheric CO_2 from root respiration (Koch, 1998; Kohn, 2010; Montañez et al., 2007; Sheldon and Tabor, 2009). Continental oxygen isotope variations ($\delta^{18}\text{O}$) in pedogenic and lake carbonates are usually linked to the composition of meteoric waters, which are strongly related to climates involving different rainfall regimes (e.g., Cerling and Quade, 1993; Talbot, 1990; Horton et al., 2016; Sheldon and Tabor, 2009). To complete the paleoenvironmental information of the Irohalene Mudstone Member, carbonates of clear pedogenic origin were obtained from nodules and rhizoconcretions of the studied pedotypes. In addition, some lacustrine materials such as carbonate mudstones, hybrid sandstones, and oolitic sandstones were also isotopically examined.

The oxygen and carbon isotope composition of inorganic carbonates is shown in Table S3. Carbonate $\delta^{13}\text{C}$ values of the pedogenic samples ranged from -5.03 of pedotype 3 and $+0.32$ of pedotype P8. $\delta^{18}\text{O}$ ranged between -2.33 observed in pedotype P7 and $+4.97$ in pedotype P8. Values for materials of palustrine origin were $\delta^{13}\text{C}$ -0.73 to $+0.62$, and $\delta^{18}\text{O}$ -0.16 to $+3.15$.

The plot of $\delta^{13}\text{C}$ versus $\delta^{18}\text{O}$ data (Fig. 10) shows that the values clustered remarkably in different genetically related groups: isotope data obtained from nodules and rhizoconcretions of P2, P3, P4, P5 and P9 pedotypes appeared clearly in Group 1, with a strong correlation ($R^2 = 0.852$; yellow and orange colors in Fig. 10). This group was composed of the Calcisols, argillic Calcisols, natric Argisols, and ferric Calcisols occurring in t5.1 of the Irohalene Member and by the Petrocalcids of P9, located in the last meters of t5.3. Another strong relationship was observed in Group 2, which includes the Vertisols and calcic Protosols of

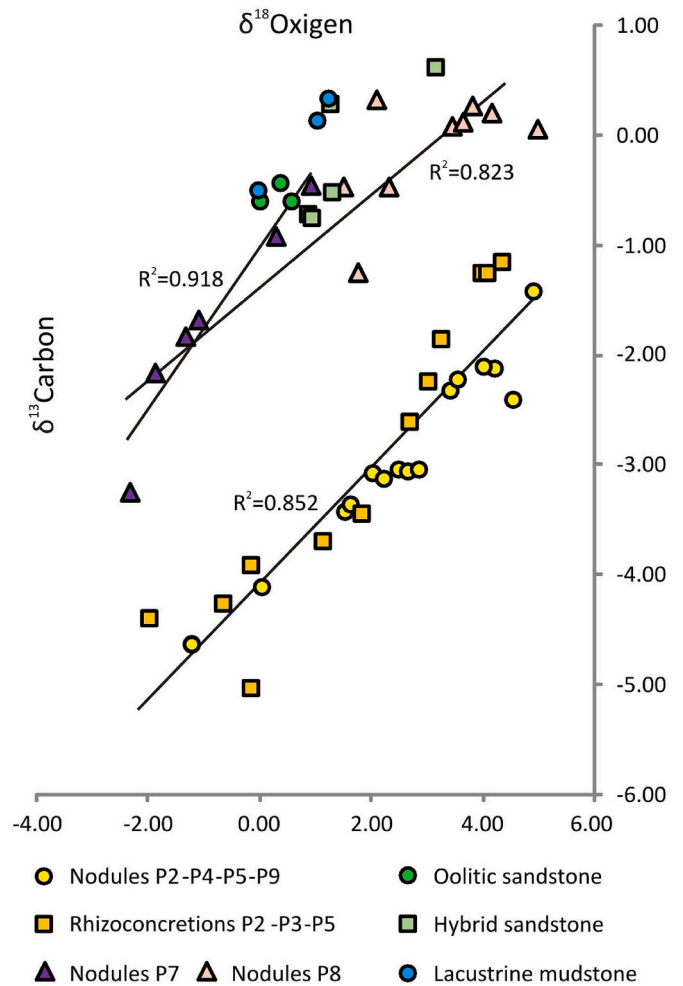


Fig. 10. Isotope data provided for carbonates as a $\delta^{13}\text{C} - \delta^{18}\text{O}$ diagram. Two groups can be differentiated. Group 1 (yellow and orange colors) includes the data obtained for pedogenic nodules and rhizoconcretions in pedotypes P2, P3, P4, P5, and P9. Group 2 is characterized by heavier $\delta^{13}\text{C}$ values recorded for nodules from P7 and P8, and related to lacustrine-palustrine environments. (For interpretation of the references to colour in this figure legend, the reader is referred to the web version of this article.)

pedotypes P7 and P8 ($R^2 = 0.823$; purple and pale pink triangles of Fig. 10). Similar paleoenvironmental conditions during carbonate precipitation would explain the clustering of the data (Cerling and Quade, 1993; Sheldon and Tabor, 2009), as indicated by the data from pedotype P7 Vertisols that, despite being separated by several meters (sampled in the upper parts of t5.2 and t5.3), showed an extremely strong correlation ($R^2 = 0.918$; purple triangles in Fig. 10). In addition, the data derived from non-pedogenic carbonates, such as hybrid sandstones, carbonate mudstones, and oolitic sandstones, appeared in the graph close to the pedotype P7 and P8 values in Group 2 (Fig. 10). It should be stressed that the isotope data of pedotype P9, which is younger than the rest of the calcareous pedotypes, fell within the trend defined by the Group 1 paleosols, therefore suggesting similar paleoenvironmental conditions. In addition, the isotope data for P8, a calcareous paleosol with similar characteristics to those of the Group 1 pedotypes, clearly followed the trend defined by Group 2 for the Vertisols of P7 and for the lacustrine materials (Fig. 10).

The $\delta^{13}\text{C}$ value of CO_2 present in soil environments is mainly affected by the isotope composition of soil waters and organic matter (Cerling, 1984). For well-drained soils in sub-humid to semi-arid climates, expected $\delta^{13}\text{C}$ values are around -4‰ to -12‰ (Tabor et al., 2017). In contrast, the isotope $\delta^{13}\text{C}$ composition of lake carbonates is usually more

positive, ranging between +3‰ and –14‰ (Talbot, 1990; Müller et al., 2006; Horton et al., 2016). The fact that Group 1 showed lighter, or more negative, $\delta^{13}\text{C}$ values than Group 2 can be explained by a change in the type of organic matter in those soils, or by a greater influence of carbonate-rich waters. This second explanation seems more plausible, considering the existing relationship of Group 2 with palustrine materials.

Expected $\delta^{18}\text{O}$ values for closed lakes under conditions of high temperatures and evaporation rates are around +3‰ (e.g., Talbot, 1990; Horton et al., 2016). Hence, the lacustrine environments of t5.2 were not characterized by low to moderate temperatures, as the isotope $\delta^{18}\text{O}$ values of their palustrine carbonates varied from –0.16 to +3.15.

8. Mineralogical characterization

Variations in the mineralogical composition of the studied sections, including bulk mineralogy and clay mineral assemblages, are shown in Fig. 11 and also detailed in the supplementary material (Table S2). Most of the samples were found to contain quartz, minor amounts of calcite, dolomite, detrital mica, hematite, albite and analcime and a clayey matrix dominated by illite, with smectite and less frequently chlorite detected in some samples. Kaolinite was not recognized in any of the samples. The full width at half maximum (FWHM) of the illite 10 Å peak in these samples indicates that they reached conditions of early diagenesis.

As a general trend, samples from the t5.1 subunit were richer in quartz (18–35%) and had relatively low calcite and dolomite contents. The clay fraction contained abundant illite sometimes with chlorite, but smectite was not identified. The t5.2 subunit showed a gradual decrease in quartz, along with a relative increase in calcite and dolomite. One of the most characteristic variations was the systematic presence of smectite (14–31%) in the clay mineral association of these samples (Fig. 12a). Interstratified illite/smectite (I/S) was only observed in some samples and appeared as an asymmetric shoulder on the low angle side of the illite 10 Å peak, which disappeared after glycolation of the oriented aggregates. The samples from subunit t5.3 first showed an increase in quartz content and decrease in the presence of smectite in the clay fraction, and this was followed by a higher calcite and smectite content of samples from the upper part of the Izarifen section.

One of the most remarkable mineralogical features was the widespread presence of analcime in most of the samples analyzed. Analcime was readily detected on X-ray diffractograms of unoriented powder (Fig. 12a). The highest contents were found in the middle part of the t5.1 subunit. However, this was not confirmed in our detailed petrographic study of thin sections, suggesting that analcime crystal sizes were sub-microscopic. SEM observations of selected samples confirmed that analcime occurs as very small (1–4 µm) subrounded (subhedral to anhedral) particles embedded in the clay matrix (Fig. 12b). These crystals frequently filled small voids among the clay particles and were also associated with relatively large dolomite rhombohedral crystals (Fig. 12c). No evidence of the replacement of feldspars, clay minerals or other mineral phases by analcime was found.

The small size of the analcime made it difficult to obtain a reliable chemical composition through both our SEM or electron microprobe study of thin sections. In most cases, our analyses revealed different degrees of contamination with surrounding minerals, and it was not possible to determine their structural formula.

The SEM study also revealed the presence of smectite as very small (<3 µm) particles together with illite and minor chlorite. Locally these particles show filamentous endings, whose composition includes some Ca and Mg. Larger mica detrital plates (up to 20 µm) and some zircon and monazite fragments are relatively frequent. Small feldspar grains often appeared aggregated and seemingly fresh (Fig. 12d). Calcite crystals were partially corroded (Fig. 9e) while the rhombohedral dolomite crystals showed well-preserved faces, although in some cases, only the mould of the crystals could be recognized.

9. Discussion

The CPE was a time of global environmental change related to substantial coeval volcanism and marine and terrestrial biological turnover (Simms and Ruffell, 1989; Benton, 1991; Dal Corso et al., 2020; Lu et al., 2021; Tomimatsu et al., 2021). The sedimentary record of the Irohalene Member is not indicative of significant volcanic activity and its fossil content basically consists of invertebrate traces, footprints and vertebrate remains. Vertebrate remains suggest a Late Triassic (Carnian) age for the Irohalene Member (Jalil and Dutuit, 1996; Jalil, 1999; Lucas, 2010; Kammerer et al., 2011). Tetrapod track composition assemblages of this member are similar in different sections of Morocco and are also similar to some ichnofaunas from North America and Central Europe (Lagnaoui et al., 2012, 2016; Zouheir et al., 2018).

Tectonic activity during the time of sedimentation of the Irohalene Member was probably not the main control on its sedimentary record, as there are not significant internal breaks in the sedimentary succession. During this time of deposition, the basin probably took the form of a wide-rift or broad sag basin (Hofmann et al., 2000; Baudon et al., 2012; Leleu et al., 2016). The present-day small dip and minor folding of the Triassic strata are the outcome of Cenozoic deformation (Medina, 1995; Mader and Redfern, 2011). Climate was thus the main control on the sedimentation of the Irohalene Member, as there is no direct evidence of proximity or marine incursion in the Argana Basin during the Late Triassic, as described for its neighboring westward Essaouira Basin (Piqué et al., 1998; Hofmann et al., 2000).

9.1. Evolution of tectonics and depositional systems

The study area is located in the northernmost zone of the Argana Basin, close to the basement high and to the faults that limited the basin during Irohalene Member deposition (Mader et al., 2017). The sedimentary record of the two studied sections reflects the proximal to distal evolution of the basin fill. The characteristics of the Had Rohala section sedimentary record indicate a closer location to the border of the basin than those of the Izarifen section (Figs. 1, 5). The general SW paleocurrent readings obtained by Mader et al. (2017) for the Irohalene Member in these areas would also corroborate this dominant transport direction.

According to the sedimentary characteristics of the Irohalene Member, this unit can be subdivided into three parts, t5.1, t5.2 and t5.3, as described by Tourani et al. (2000) and Hofmann et al. (2000) (Fig. 2). The first part t5.1 includes the lower 57 m and 68 m of the Had Rohala and Izarifen sections respectively (Fig. 5). This lower part is well-correlated according to the characteristics of some paleosols. It is basically represented by mid dry-land fluvial systems with substantial development of overbank and floodplain deposits, where crevasse splay and meandering systems are the main architectural elements. The oldest part of the member only appears in the Had Rohala section, and makes contact with the t4 Member (Beauchamp, 1988; Tourani et al., 2000). These first deposits show GB, SB, CH and CR as dominant architectural elements, related to more proximal areas where paleocurrent readings indicate a SW direction (Figs. 5, 6e). When compared, the vertical succession of the differentiated architectural elements in this lower part of the member, the Had Rohala section shows a greater interconnectivity between them. This could indicate an alluvial environment closer to the drainage basin with higher rates of erosion (Schumm, 1977), similar to the lateral evolution described by Legarreta and Uliana (1998) in Early Cretaceous fluvial systems in the Neuquen Basin, Argentina.

The second differentiated part t5.2, or middle part, of the Irohalene Member only crops out in the Izarifen section. This part is about 92 m thick (Figs. 5, 6e). The beginning of this middle part shows a significant change with respect to the lower part of the member. It is basically represented by LCc and LCs architectural elements (Fig. 5) which sedimentary and paleosol characteristics mainly point to the development of carbonate and siliciclastic humid lacustrine environments. These

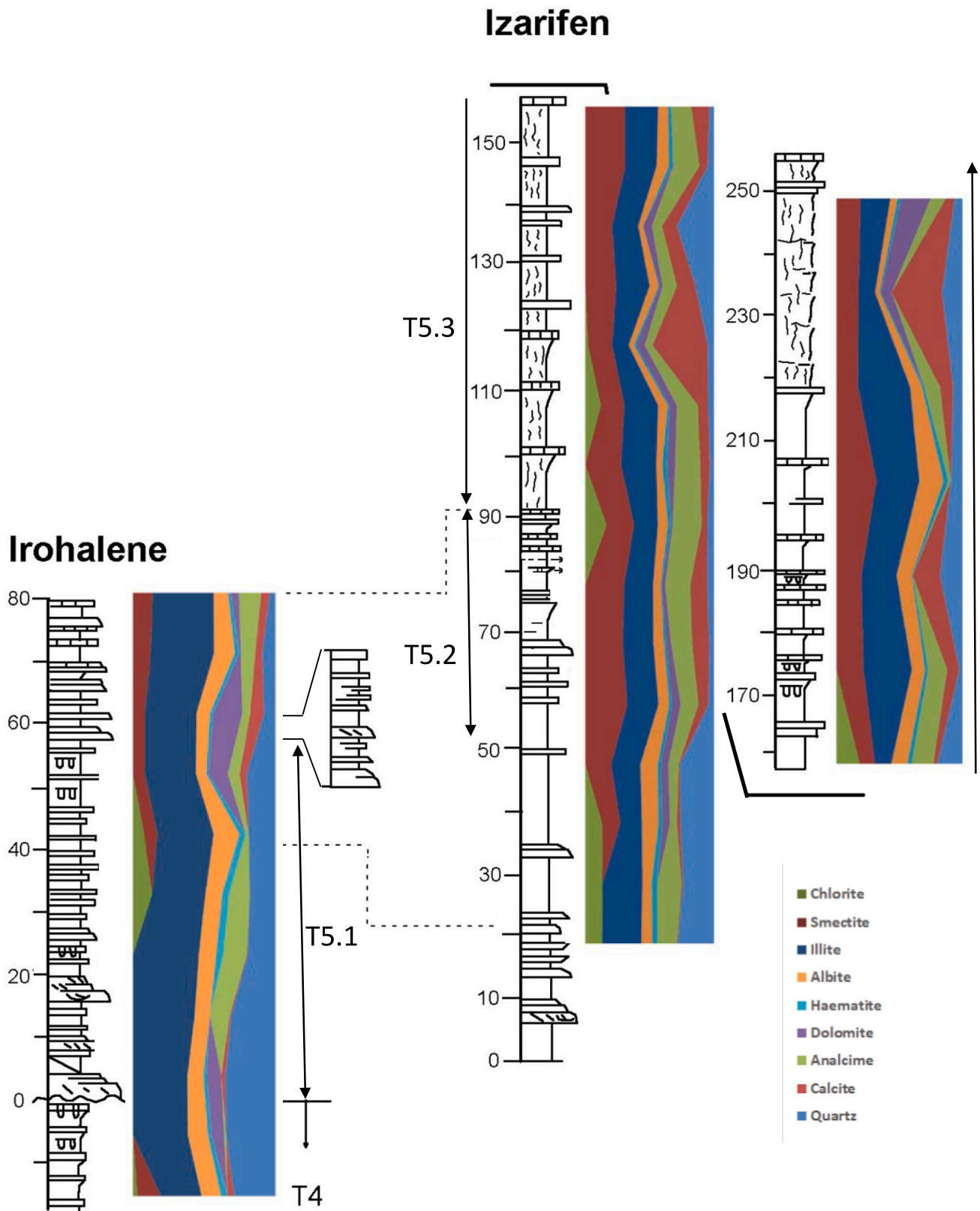


Fig. 11. Variations in mineralogic compositions across subunits t5.1 to t5.3 in the two sections studied. Semi-quantitative estimates based on XRD data (non-oriented powder and oriented aggregates). Note that illite is the only clay mineral present in the t5.1 subunit, which, in turn, shows the highest quartz and analcime contents. Smectite appears at the start of the t5.2 subunit, where the highest contents occur, while this mineral shows greater variation in t5.3.

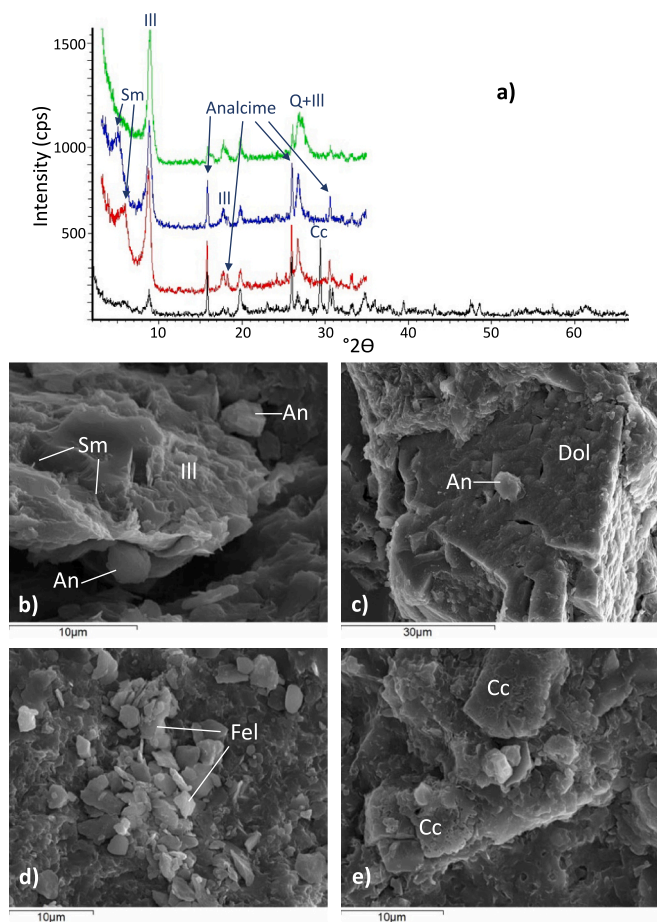


Fig. 12. a) XRD patterns recorded in sample IZA 5 obtained from the t5.2 subunit, including diffractograms of air-dried oriented aggregates, OA (AD), solvated with ethylene-glycol, OA (EG) and heated to 550 °C, OA (TT). Peaks labeled are smectite (Sm), illite (Ill), analcime, calcite (Cc) and quartz (Q). b) to e) Scanning electron microscope (SEM) images of selected samples b) Sub-rounded analcime (An) particles (<4 μm) were found in small voids within the clayey matrix formed by illite and filamentous smectite. c) A small analcime particle on the surface of a larger dolomite crystal. d) Aggregate of fresh K-feldspar (Fel) grains surrounded by an illite matrix. e) Partially corroded calcite crystals showing small cavities formed by dissolution.

conditions allowed for the development of fauna both in the interior of the ponds and soils of wetter conditions in the surrounding floodplain environments. Similar changes to wetter conditions were described in lakes, which developed into floodplains, by Bennett et al. (2016) in the Carboniferous of Southern Scotland. As the result of a possible decrease in subsidence and increased humidity and sediment flows, more lateral extensive and less oxidized (red) silt, fine-grain sand and carbonate bodies were deposited under conditions of perennial or semi-perennial flows (Dalrymple et al., 1998) in the middle part of the Irohalene Member (Fig. 6e).

The upper part of the Irohalene Member t5.3 only shows a complete record in the Izarifen section. This part is about 105 m thick (Fig. 5, 6e). While this part is, again, basically represented by LCs and LCs architectural elements, there is a considerable difference in the sedimentary environment from that of the middle part. In the upper part, the reduced thickness of LCs and LCs elements and their interconnectivity is accompanied by an increase in oxidation conditions, indicated by root traces with thinner haloes and sedimentary structures such as desiccation cracks indicating subaerial exposure. These features suggest decreased humidity and energy in flows, pointing to the development of an extensive floodplain in distal and arid conditions. Similar examples

have been described in floodplain fines by Gulliford et al. (2017) in the Permian Beauford Group, South Africa.

9.2. Mineralogy, paleosols and climatic evolution

As mentioned above, one of the most remarkable findings of our mineralogical study was the presence of varying proportions of smectite (together with illite) in the clay mineral assemblage in most of the samples of subunits t5.2 and t5.3. However, the clay mineralogy of the t5.1 subunit samples consists almost exclusively of illite (and minor chlorite). The presence or absence of smectite needs to be carefully considered, as it could shed light on the paleoenvironmental conditions that prevailed during the deposition of these sediments. It is therefore important to find textural and compositional criteria that will help discriminate the origin of these mineral phases in the Argana samples.

The FWHM of the 10 Å peak indicates that these rocks reached early diagenesis conditions and suggests a limited extent of deep burial or deformation-related transformations of the clay mineral assemblage, which allows us to discuss whether they are the result of paleoclimatic/paleoenvironmental variations or of alteration of pre-existing minerals. Accordingly, the presence of smectite in some layers (in t5.2 and t5.3 subunits) may be related to periods of relatively warm climate and marked seasonality between wet and dry periods, or it may be linked to the alteration of glass and ash of volcanic origin (Chamley, 1989). In our detailed SEM study of selected samples from the different sections, no evidence of volcanic precursors was found that could have promoted the formation of smectite through alteration. Smectite occurs as very small (<3 μm) particles that form the clayey matrix together with illite and, to a lesser extent, chlorite. Locally it was possible to find small particles with filamentous endings, whose composition includes some Ca and Mg, suggesting they could correspond to smectite. Therefore, the origin of the smectite is probably not related to alteration of volcanic glass or ash, but its formation in this case is indicative of direct precipitation under suitable (wetter) climatic conditions.

As discussed below, the sedimentological characteristics and paleosol types described for subunit t5.1 suggest their formation in an arid climate with little rainfall, which would be compatible with the presence of illite and the absence of smectite in their mineralogical composition. According to these sedimentological and paleosol data (isotopes, etc.), the beginning of the t5.2 subunit was marked by a considerable increase in humidity, which would explain the presence of smectite coinciding with these changes. Variations in smectite content in both the t5.2 and t5.3 subunits are consistent with more humid or arid climatic conditions inferred from sedimentological and paleosol characteristics. Accordingly, the presence or absence of smectite probably reflects a change to a wetter or more arid paleoclimate, respectively.

In addition, most of the samples collected in both sections contained analcime. This mineral is commonly described in sedimentary rocks of both continental and marine origin. In lacustrine sediments it is generally linked to the alteration of volcanogenic materials or other zeolites (Surdam and Sheppard, 1978; Iijima, 1980; Hay and Sheppard, 2001), although it can also form via direct authigenic precipitation from lake-water/porewater in alkaline lake sediments, or through the reaction of these waters with clay minerals or plagioclase (Gall and Hyde, 1989; Do et al., 2007). In most of the analyzed samples from the Argana sections, analcime occurs as submicroscopic particles (< 4 μm) which tended to fill small vugs within the clay matrix. No evidence of alteration of volcanogenic materials was detected, nor were transformation processes of other zeolites observed, so we consider that it was probably formed by direct precipitation from alkaline waters. The small size of analcime particles means their composition cannot be reliably established. However, considering their other characteristics, they can be assigned to the Group C defined by Coombs and Whetten (1967) of analcimes of silica-poor composition that coexist with precipitated dolomite in rocks where there is no evidence of the presence of volcanic glass.

The textural characteristics and mineralogical composition of the

Argana samples were similar to those described by Gall and Hyde (1989) for Carboniferous lacustrine sediments from Newfoundland (Canada), where analcime occurs together with phyllosilicates (illite, smectite, interstratified I/S and chlorite), quartz, feldspar, calcite and dolomite. These authors suggested that analcime was formed through the precipitation of lacustrine waters rich in sodium or interstitial waters in partially lithified sediments. A similar origin was proposed by Do et al. (2007) for analcime in samples from a Paleogene fluvial-lacustrine sequence in northwestern Argentina. This is the most probable formation mechanism for analcime in our Argana samples. In fact, the highest analcime contents were detected in the levels where natric soils develop, that is, subunit t5.1 (Table S2). In addition, there was good correlation between Na₂O contents determined by whole rock chemical analysis and the analcime proportion estimated by XRD (Fig. 13), suggesting that most of the sodium in the samples could be attributed to analcime. This notion supports the idea that analcime probably precipitated as a primary phase, and that the proportion of analcime reflects variations in the Na₂O contents of these alkaline lake waters.

Regarding the study of paleosols and their comparison with other areas, in their review of the CPE in the northern Central European Basin, Franz et al. (2019) described a wide array of paleosols in the Stuttgart Formation that included Protosols, Spodosols, Histosols, Vertisols, Calcisols, and Gypsisols. These authors did not observe a clear distribution of paleosols over time and instead related the different pedotypes with the lateral development of depositional environments in transgressive-regressive phases. Thus, hydromorphic Protosols, Histosols and Spodosols were found mainly in delta plains wetlands of the final stage of the transgression phase, and well-drained Calcisols, Gypsisols and Vertisols in the distributive fluvial systems and channel-floodplain systems of the regression phase. Those authors did not recognize a humid mid-Carnian episode and related the widespread occurrence of vertisols, calcisols and gypsisols as evidence of a climate with high evaporation rates exceeding precipitation rates. In eastern Spain, Barrenechea et al. (2018) described a change from gleyed Protosols to gleyed Calcisols and suggested elevated water tables and a slightly more humid climate without substantial rainfall episodes. However, in the northwest of Argentina, the Chañares–Los Rastros succession records a change from fluvial sandy deposits with root traces and small carbonate concretions towards lacustrine strata of warmer and more humid conditions deposited during or after the CPE (Mancuso et al., 2020; Benavente et al., 2022). This transition is very similar to that observed between the t5.1 and t5.2

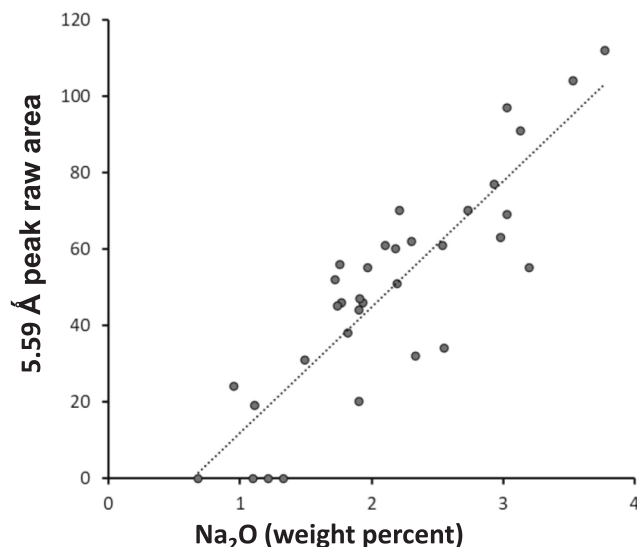


Fig. 13. Plot of the Na₂O contents determined in chemical analyses on whole sample versus the raw area of the analcime 5.59 Å peak in XRD traces of unoriented powders.

subunits. The transition between the Los Rastros and Ischigualasto formations in western Argentina was studied by Mancuso et al. (2022), highlighting an increase in moisture in the upper part of the latter unit. Taking into account the existing age limitations, this increase in precipitation could be related to the second wet pulse that we described in the Argana basin, although additional data and more precise ages are needed to confirm this equivalence. Finally, in the Tofane area in the Dolomites of Italy the CPE is detected by the presence of paleosols with a spodic horizon under an overlying histic (rich in organic matter) horizon (Breda et al., 2009).

In the Irohalene Member there is a clear distribution over time of the differentiated pedotypes that fit well with the sedimentologic and mineralogic data. Subunit t5.1 was characterized by pedotypes P2, P3, P4, and P5, which showed carbonate contents in their subsurface horizons. Probably, the most characteristic paleosol was P4, with its natric horizon including domed columnar ped structures, similar to those described by McCahon and Miller (1997) for the Permian of north-central Kansas. Natric horizons are typical of arid and semiarid environments (Soil Survey Staff, 1999; McCahon and Miller, 1997; Retallack, 2001).

The calcareous and nodular paleosols of t5.1 were replaced in t5.2 by the Vertisols of P6 and P7, which occurred related to sediments of lacustrine environments integrated into the architectural elements LCs and LCc. Pedotypes P6 and P7 were smectitic Vertisols (Fig. 14) showing evident slickenside structures and Gilgai microrelief (Figs. 10H, 11A, B) created by swelling and shrinking processes due to volume and water content changes. Similar Vertisols are typically observed in semi-arid to humid climates (Soil Survey Staff, 1999; Nordt et al., 2004; Nordt and Driese, 2009). Section t5.2 is characterized also by an increase in MgO and CaO contents, probably related to seasonally infiltration of waters rich in calcium carbonate of ponds into the soils as observed in the palustrine materials of early Permian age from northern Iberia (López-Gómez et al., 2021), and by an increasing trend in Fe₂O₃ contents (Fig. 14). In Vertisols formed under humid climate conditions, increased iron contents have been related to higher rainfall (Nordt and Driese, 2009). In addition, section t5.2 showed high Ba/Sr and CIA-K ratios (Fig. 14). The Ba/Sr ratio represents leaching behavior during weathering (Sheldon and Tabor, 2009), and high values in the B horizons of paleosols represent more leaching. Similarly, the chemical index of alteration without potassium (CIA–K) of Maynard (1992) is commonly used as an indicator of chemical weathering and humidity (Sheldon and Tabor, 2009). The CIA–K index correlates well with mean annual precipitation (MAP) as determined through the geochemical climofunction of Sheldon et al. (2002). High MAP values of 1129 mm were observed here in the lower part of t5.2 (Fig. 14; Table S1). Unfortunately, both Ba/Sr and CIA–K ratios were lower for t5.2 than expected. This is likely because of the complex mechanical behavior of Vertisols (Nordt et al., 2004; Nordt and Driese, 2009). In addition, these ratios are useful for well-drained soils but more ineffective for gleyed paleosols or those containing carbonate-rich sediments (Tabor and Myers, 2015; Golberg and Humayun, 2010), as was the case for many zones in t5.2.

Notwithstanding, humid conditions for t5.2 were better explained by our isotope carbon and oxygen data. As observed earlier in Fig. 10, isotope data clustered in two groups. The isotopically lighter Group 1 data were derived from nodules and rhizoconcretions found in well-drained paleosols, and the Group 2 data corresponded to small nodules of Vertisols and calcic Protosols that were probably affected seasonally by isotopically heavier carbonate-rich waters (see Tabor et al., 2017; Talbot, 1990; Müller et al., 2006; Horton et al., 2016). A greater amount of water in t5.2 could explain the distribution of our isotopic data as two well-differentiated groups (Fig. 10).

Climate has a huge impact on the carbon and oxygen isotope composition of soils, such that δ¹³C and δ¹⁸O values are heavier for arid than humid environments (Deines, 1980; Sikes and Ashley, 2007; Sheldon and Tabor, 2009; Kohn, 2010; Dal Corso et al., 2012; Horton et al., 2016; Mancuso et al., 2020). When our isotope data were analyzed

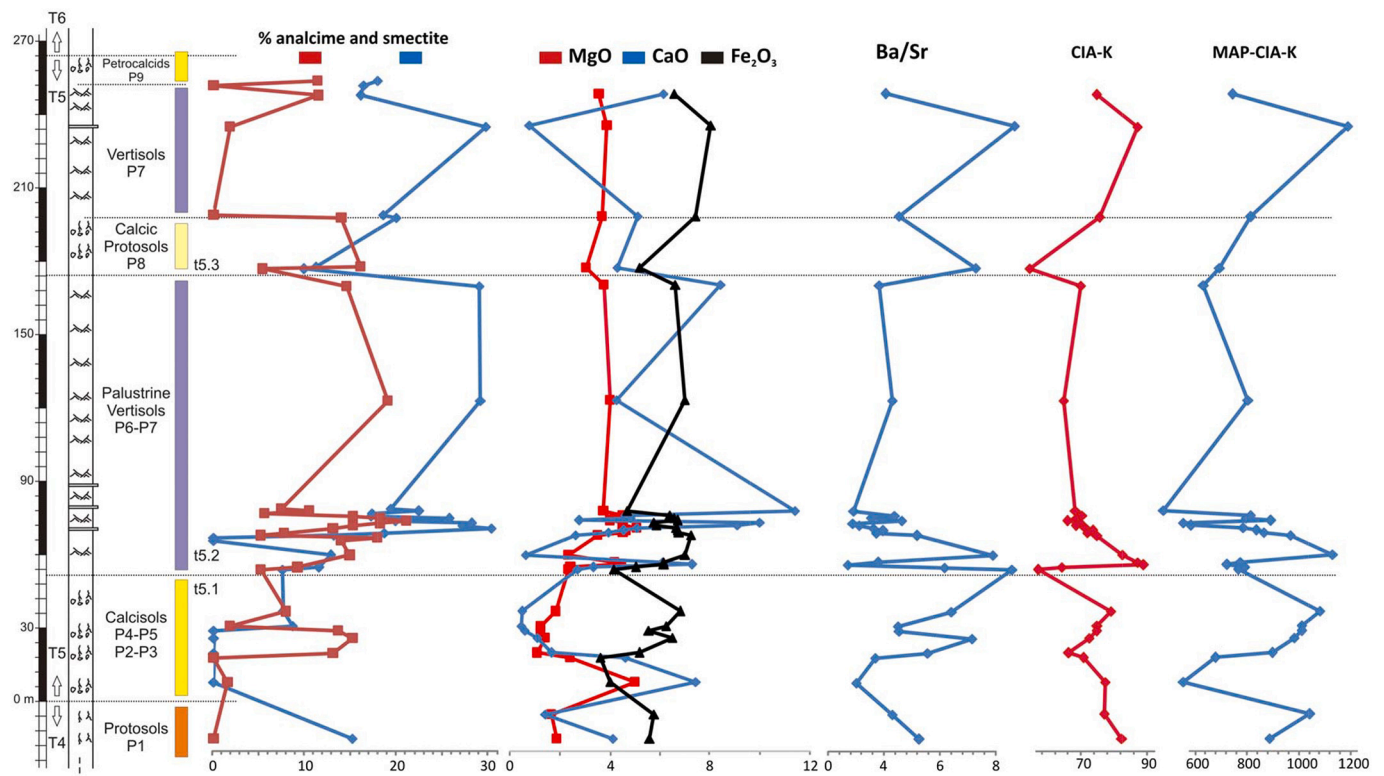


Fig. 14. Main mineralogical and geochemical features of t5.1, t5.2, and t5.3 of the Irohalene Member. See original data in Tables S1 and S2.

stratigraphically (Fig. 15), we were able to identify two trends towards more arid conditions. One was observed in t5.1 and the other in the lower part of t5.3. A third arid trend is starting to emerge at the very top of t5.3, but we do not have sufficient data to confirm this.

The first two aridity trends were interrupted by two humid intervals that do not show pedogenic developments with substantial carbonate accumulations in the form of nodules. For these humid periods, data were obtained from palustrine carbonate muds and from small nodules in two profiles of pedotype P7, at the top of t5.2 and t5.3 (Fig. 15). As mentioned above, lacustrine-palustrine carbonate muds offer heavier isotopic compositions than purely pedogenic carbonates. Therefore, it is important to compare the pedogenic carbonates of t5.1 with the data obtained from the Vertisols of P7 and not with those obtained from palustrine materials. Although there may be influence of carbonated waters in the gleyey Vertisols of P7, those located at the top of t5.2 displayed lighter isotope compositions than some of the paleosols in t5.1, suggesting more humid conditions.

According to the $\delta^{18}\text{O}$ data obtained for the palustrine environments of t5.2, it is difficult to ascribe a temperate climate with heavy rainfall to this subunit. Oxygen isotope data were quite high, similar to those obtained for closed lakes in conditions of high temperatures and evaporation rates, which may reach positive $\delta^{18}\text{O}$ values of around 3‰ (e.g., Talbot, 1990; Horton et al., 2016). However, the amount of available water was probably increased with respect to t5.1, occasionally flooding the landscape and preventing the existence of well-drained soils. Increased meteoric waters from local rainfall would explain the sedimentologic, mineralogic, and isotope data of t5.2. On the other hand, the isotope $\delta^{18}\text{O}$ data recorded in the Irohalene Member, indicated a general trend towards higher temperatures (Fig. 15), probably related to more arid conditions, which was interrupted by two humid but hot intervals, the first of these being the most important in terms of the presence of water in the system.

Our sedimentology, clay mineralogy and paleosol studies carried out in the Irohalene Member reveal that this unit experienced peaks of increased humidity during its deposition. These changes were basically

concentrated in the time interval represented by the middle part of the member, although new humid conditions appeared again in the upper part of the unit. This increase in humidity conditions reflects a change in the generally arid conditions developing in the Argana Basin during the Late Triassic. The most humid conditions formed in the t5.2 interval, where a clam shrimp association indicated a Carnian age, probably late Julian-early Tuvalian age, allowing us to attribute this humid interval to the CPE. Widespread arid and semi-arid conditions, as shown in t5.1 and part of the upper t5.3 interval, indicate that this CPE was not a single humid interval, but was represented by different pulses, as described in other western Tethys continental examples (eg., Arche and López-Gómez, 2014; Barrenechea et al., 2018; Stefani et al., 2010; Roghi et al., 2010; Dal Corso et al., 2018). These results agree with those recently obtained by Zouheir et al. (2023) also in the Irohalene Member. Different pulses of arid and semi-arid conditions have been also recorded in many marginal marine and marine examples (Preto and Hinnov, 2003; Breda et al., 2009; Stefani et al., 2010; Roghi et al., 2010; Dal Corso et al., 2018; Baranyi et al., 2019).

10. Conclusions

The Carnian Pluvial Episode, or short humid episode, occurring during the Julian to Tuvalian of the Carnian, is described here for the first time in the Argana Basin, Western High Atlas, Morocco. This was a multidisciplinary study based on the biostratigraphy, sedimentology, paleosols, geochemistry and clay mineralogy of its sections Had Rohala and Izarifien.

Precise age data based on a clam shrimp association were obtained for the Irohalene Member or t5 unit, and are here presented to define this time interval. This association of clam shrimp was characterized by the presence of *Laxitextella laxitexta* Sandberger, 1871, *Laxitextella multireticulata* Reible, 1962, *Laxitextella* sp., *Howellisaura princetonensis* Bock, 1953, *Euestheria minuta* von Zieten, 1833, *Euestheria* spp. and *Gregorisuella* sp.

Based on sedimentary analyses including the differentiation of facies,

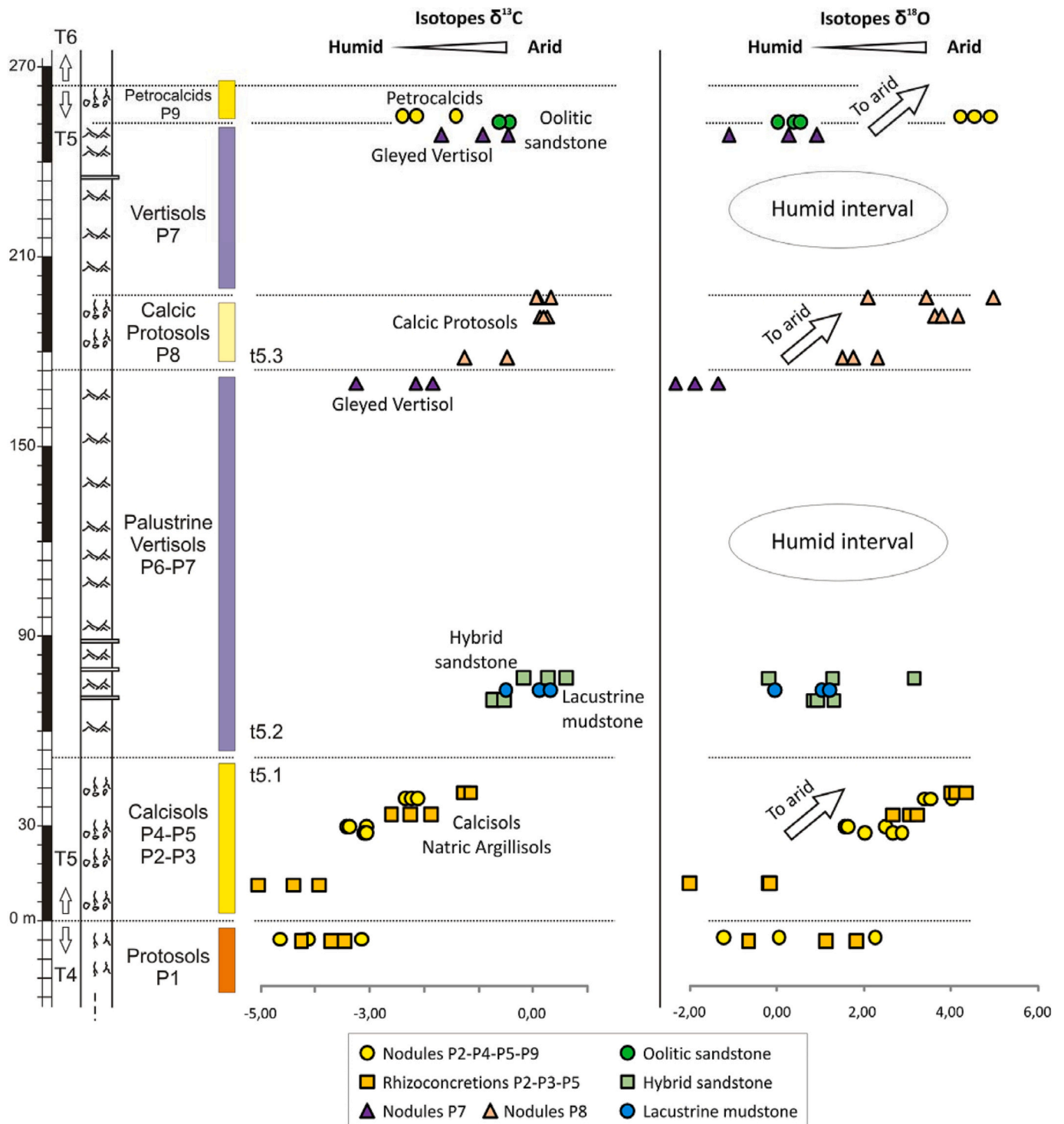


Fig. 15. Isotope ($\delta^{13}\text{C} - \delta^{18}\text{O}$) data vertically arranged through the stratigraphic section. The Irohalene Member is characterized by two humid intervals. Palustrine materials and Vertisols served to differentiate between periods of arid conditions. See text for explanations.

facies associations, architectural elements, and correlations, the Irohalene Member can be subdivided vertically into three parts t5.1, t5.2 and t5.3. The lower t5.1 part is composed by gravel bars and channels related to proximal areas, fluvial meandering systems and overbank and floodplains deposits. The middle t5.2 and upper t5.3 parts mainly contain floodplain deposits where siliciclastics and carbonate ponds developed.

The widespread presence of analcime in most of the samples results from primary precipitation of lacustrine waters rich in sodium or

interstitial waters in the sediments. The proportion of analcime reflects variations in the Na_2O contents of these alkaline lake waters.

The sedimentary characteristics of the middle t5.2 section indicate more permanent water and general humid conditions, which were also suggested by a drastic change in the type of paleosols and in the mineralogy of their materials. The calcareous and well-drained pedotypes of t5.1 disappeared and were replaced in t5.2 by smectitic Vertisols related to flooded environments. The presence of smectite in some layers in this case is indicative of direct precipitation under wetter

climatic conditions.

Stable carbon and oxygen isotope compositions of soil and palustrine carbonates were indicative of a general tendency towards arid conditions, which was interrupted by two intervals characterized by more humid yet hot conditions, as observed in studies carried out in other areas for this time interval.

Declaration of Competing Interest

The authors declare that they have no known competing financial interests or personal relationships that could have appeared to influence the work reported in this paper.

Data availability

Data will be made available on request.

Acknowledgements

The authors thank Ana Burton for editorial assistance. Funds were provided by project PGC2018-098272-B-I00 (Spanish Ministry of Science, Innovation and Universities) and PI18Q005 (Secretaría General de Ciencia y Técnica, UNNE) and PIP-11220150100117CO del Consejo Nacional de Investigaciones Científicas y Técnicas (CONICET). Also, thanks to Dr. Mateo D. Monferran (CECOAL-CONICET-UNNE, Corrientes, Argentina) and Geol. Carlos M. Alarcón Gómez (CIGEOBIO, San Juan, Argentina) for helping with clam shrimps studies and figures. We thank Dr. Olivier Béthoux (MNHN, Paris) for taking the RTI photos of the clam shrimps association, and N-E. Jalil and J. Desojo for their invaluable help during the first phase of the study of the paleontological material. The staff of the C.A.I. of Geological Sciences of the Complutense University in Madrid helped during the S.E.M. study. We also thank the two anonymous reviewers for improving this final version with their insightful comments.

Appendix A. Supplementary data

Supplementary data to this article can be found online at <https://doi.org/10.1016/j.palaeo.2023.111720>.

References

- Arche, A., López-Gómez, J., 2014. The Carnian pluvial event in Western Europe: new data from Iberia and correlation with the western Neotethys and eastern North America–NW Africa regions. *Earth-Sci. Rev.* 128, 196–231.
- Baranyi, V., Rostási, A., Raucsik, B., Michael, W., 2019. Palynology and weathering proxies reveal climatic fluctuations during the Carnian Pluvial Episode (CPE) (late Triassic) from marine successions in the Transdanubian Range (western Hungary). *Glob. Planet. Change* 177, 157–172.
- Barrenechea, J., López-Gómez, J., De la Horra, R., 2018. Sedimentology, clay mineralogy and palaeosols of the Mid-Carnian Pluvial Episode in eastern Spain: insights into humidity and sea-level variations. *J. Geol. Soc. Lond.* 175, 993–1003.
- Baudon, C., Redfern, J., Den Driessche, Van, 2012. Permo-Triassic structural evolution of the Argana Valley, impact of the Atlantic rifting in the High Atlas, Morocco. *J. Afr. Earth Sci.* 65, 9191–104.
- Beauchamp, J., 1988. Triassic sedimentation and rifting in the High Atlas (Morocco). In: Manspeizer, W. (Ed.), *Triassic-Jurassic Rifting. Developments in Geotectonics*, 22, pp. 477–497.
- Benavente, C.A., Mancuso, A.C., Irmis, R.B., Bohacs, K.M., Matheos, S., 2022. Tectonically Conditioned Record of Continental Interior Paleoclimate during the Carnian Pluvial Episode: The Upper Triassic Los Rastros Formation, Argentina. *Geol. Soc. Am. Bull.* 134 (1–2), 60–80. <https://doi.org/10.1130/B35847.1>.
- Bennett, C.E., Kearsey, T.I., Davies, S.J., Millward, D., Clack, J.A., Smithson, T.R., Marshall, J.E.A., 2016. Early Mississippian sandy siltstones preserve rare vertebrate fossils in seasonal flooding episodes. *Sedimentology* 63, 1677–1700.
- Benton, M.J., 1986. More than one event in the late Triassic mass extinction. *Nature* 321, 857–861.
- Benton, M.J., 1991. What really happened in the late Triassic? *Hist. Biol.* 5, 263–278.
- Benton, M.J., Bernardi, J., Kinsella, C., 2018. The Carnian Pluvial Episode and the origin of dinosaurs. *J. Geol. Soc.* 175, 1019–1026.
- Benton, M.J., Ford, J., Langer, M., 2014. Models for the rise of dinosaurs. *Curr. Biol.* 24, 87–95.
- Bernardi, M., Gianillo, P., Petti, F.M., Mietto, P., Benton, M.J., 2018. Dinosaur diversification linked with the Carnian Pluvial Episode. *Nat. Commun.* 9 (1499), 1–10.
- Blackburn, T.J., Olsen, P.E., Bowring, S.A., McLean, N.M., Kent, D.V., Puffer, J., McHone, G., Rasbury, E.T., Et-Touhami, M., 2013. Zircon U-Pb Geochronology Links the End-Triassic Extinction with the Central Atlantic Magmatic Province. *Science* 340, 941–945. <https://doi.org/10.1126/science.1234204>.
- Bluck, B.J., 1971. Sedimentation in the meandering river Endrick. *Trans. R. Soc. Edinburg* 70, 181–220.
- Breda, A., Preto, N., Roghi, G., Furin, S., Meneguolo, R., Ragazzi, E., Fedele, P., Gianolla, P., 2009. The Carnian Pluvial Event in the Tofane area (Cortina d'Ampezzo, Dolomites, Italy). *Geol. Alp* 6, 80–115.
- Bridge, J., Demicco, R., 2008. *Earth Surface Processes, Landforms and Sediment Deposits*. Cambridge University Press, Cambridge.
- Brown, R.H., 1980. Triassic rocks of the Argana valley, Southern Morocco, and their regional structural implications. *Am. Assoc. Pet. Geol. Bull.* 64, 988–1003.
- Buffa, V., Jalil, N.-E., Steyer, J.-S., 2019. Redescription of *Arganasaurus* (*Metoposaurus*) *azerouali* (Dutuit) comb. Nov. From the Upper Triassic of the Argana Basin (Morocco), and the first phylogenetic analysis of the *Metoposauridae* (Amphibia, Temnospondyli). *Papers. Palaeontology* 5 (4), 1–19.
- Burns, C.E., Mountney, N.P., Hodgson, D.M., Colomera, L., 2017. Anatomy and dimensions of fluvial crevasse-splay deposits: examples from the cretaceous Castlegate Sandstone and Neslen Formation, Utah, U.S.A. *Sediment. Geol.* 351, 21–35.
- Cerling, T.E., Quade, J., 1993. Stable Carbon and Oxygen Isotopes in Soil Carbonates. In: Swart, P.K., Lohmann, C.K., McKenzie, J., Sarin, S. (Eds.), *Climate Change in Continental Isotopic Records*. American Geophysical Union, Washington, DC, Geophysical Monograph, pp. 217–232. <https://doi.org/10.1029/GM078p0217, 78> pp.
- Cerling, T.E., 1984. The stable isotopic composition of modern soil carbonate and its relationship to climate. *Earth Planet. Sci. Lett.* 71, 229–240. [https://doi.org/10.1016/0012-821X\(84\)90089-X](https://doi.org/10.1016/0012-821X(84)90089-X).
- Chamley, H., 1989. *Clay Sedimentology*. Springer, Berlin.
- Coombs, D.S., Whetten, J.T., 1967. Composition of analcime from sedimentary and burial metamorphic rocks. *Geol. Soc. Am. Bull.* 78, 269–282. [https://doi.org/10.1130/0016-7606\(1967\)78\[269:COAFSA\]2.0.CO;2](https://doi.org/10.1130/0016-7606(1967)78[269:COAFSA]2.0.CO;2).
- Courel, L., Ait Salem, H., Benaouiss, N., Et-Touhami, M., Fekirine, B., Oujidi, M., Soussi, M., Tourani, A., 2003. Mid-Triassic to early Liassic clastic/evaporitic deposits over the Maghreb Platform. *Palaeogeogr. Palaeoclimatol. Palaeoecol.* 196 (1–2), 157–176.
- Daffaut, F., Brun, L., Planchut, B., 1966. Le bassin du Sud-Ouest marocain. I. In: Reyre, D. (Ed.), *Bassins sédimentaires du littoral africain*. Symposium New Delhi, 1964. Publication des Associations de Services Géologiques Africains, Paris, pp. 5–26, 1er partie.
- Dal Corso, J., Mietto, P., Newton, R.J., Pancost, R.D., Preto, N., Roghi, G., Wignall, P.B., 2012. Discovery of a major negative $\delta^{13}C$ spike in the Carnian (Late Triassic) linked to the eruption of Wrangellia flood basalts. *Geology* 40, 79–82.
- Dal Corso, J., Gianolla, P., Newton, R.J., Franceschi, M., Roghi, G., Caggiati, M., Raucsik, B., Budai, T., Haas, J., Preto, N., 2015. Carbon isotope records reveal synchronicity between carbon cycle perturbation and the “Carnian Pluvial Event” in the Tethys realm (Late Triassic). *Glob. Planet. Change* 127, 79–90.
- Dal Corso, J., Gianolla, P., Rigo, M., Franceschi, M., Roghi, G., Mietto, P., Manfrin, S., Raucsik, B., Budai, T., Jenkyns, H.C., Raymond, C.E., Caggiati, M., Gattolin, G., Breda, A., Merico, A., Preto, N., 2018. Multiple negative carbon-isotope excursions during the Carnian Pluvial Episode (Late Triassic). *Earth-Sci. Rev.* 185, 732–750.
- Dal Corso, J., Bernardi, M., Sun, Y., Song, H., Seyfullah, L.J., Preto, N., Gianolla, P., Ruffell, A., Kustatscher, E., Roghi, G., Merico, A., Höhn, S., Schmidt, A.R., Marzoli, A., Newton, R.J., Wignall, P.B., Benton, M.J., 2020. Extinction and dawn of the modern world in the Carnian (Late Triassic). *Sci. Adv.* 6 (38), eaba0099.
- Dalrymple, M., Prosser, J., Williams, B., 1998. A dynamics systems approach to the regional controls on deposition and architecture of alluvial sequences, illustrated in the Stratford Formation (United Kingdom, northern North Sea). In: Shanley, K.W., McCabe, P.J. (Eds.), *Relative Role of Eustasy, Climate, and Tectonism in Continental Rocks*, 59. SEPM Special Publication, pp. 65–82.
- De Haas, T., Van der Berg, W., Braat, L., Kleinhans, G., 2016. Autogenic avulsión, channelization and backfilling dynamics of debris-flow fan. *Sedimentology* 63, 1596–1619.
- Defretin, S., 1950. Sur quelques *Estheria* du trias français a facies germanique et de l'Hettangien. *Ann. Soc. Geol. Nord* 70, 214–227.
- Defretin, S., Fauvelet, E., 1951. Présence de phyllopoques triasiques dans la région d'Argana-Bigoudine (Haut-Atlas occidental). *Notes. Mem. Serv. Geol.* 85, 129–135.
- Deines, P., 1980. The isotopic composition of reduced organic carbon. In: Fritz, P., Fontes, J.C. (Eds.), *Handbook of Environmental Isotope Geochemistry. The Terrestrial Environment*. Elsevier, pp. 329–406.
- Do, Campo M., del Papa, C., Jiménez-Millán, J., Nieto, F., 2007. Clay mineral assemblages and analcime formation in a Palaeogene fluvial-lacustrine sequence (Maíz Gordo Formation Palaeogen) from northwestern Argentina. *Sediment. Geol.* 201, 56–74. <https://doi.org/10.1016/j.sedgeo.2007.04.007>.
- Dutuit, J.M., 1976. Introduction à l'étude paléontologique du Trias continental marocain. Description des premiers Stégocephales recueillis dans le couloir d'Argana (Atlas occidental). *Mém. Mus. Natl. d'Hist. Nat. Paris Sér. C* 36, 1–253.
- Dutuit, J.M., 1977a. *Paleorhinus magnoculus*, Phytosaure du Trias supérieur de l'Atlas marocain. *Ann. Univ. Provence Géol. Méditerranéenne* 4 (3), 255–267.
- Dutuit, J.M., 1977b. Description du crâne de *Angistorhinus talanti* n. sp. Un nouveau phytosaure du Trias atlasique marocain. *Bull. Mus. Natl. Hist. Nat. Paris Sér.* 489, 297–324.

- Duval-Arnould, A., Schröder, S., Charton, R., Joussiaume, R., Razin, P., Redfen, J., 2021. Early post-rift depositional systems of the Central Atlantic: lower and Middle Jurassic of the Essaouira-Agadir Basin, Morocco. *J. Afr. Earth Sci.* 178, 104–164. <https://doi.org/10.1016/j.jafrearsci.2021.104164>.
- Ebert, D.A., Miall, A.D., 1991. Stratigraphy, sedimentology and evolution of a vertebrate-bearing, braided to anastomosed fluvial system, Cutler Formation (Permian-Pennsylvanian), North-Entral Mexico. *Sediment. Geol.* 72, 225–252.
- Farrell, K.M., 1987. Sedimentary and facies architecture of overbank deposits of the Mississippi River, False River Region, Louisiana. In: Ethridge, F.G., Flores, R.M., Harvey, M.D. (Eds.), *Soc. Econ. Paleontol. Mineral. Spec. Publ.* 39, pp. 111–120.
- Foix, N., Paredes, J.M., Giacosa, R.E., 2013. Fluvial architecture variations linked to changes in accommodation space: Río Chico Formation (Late Paleocene), Golfo San Jorge Basin, Argentina. *Sediment. Geol.* 294, 342–355.
- Forbes, D.L., 1983. Morphology and sedimentology of a sinuous gravel-bed channel system, lower Babbage River, Yokon coastal plain, Canada. In: Collinson, J.D., Lewin, J. (Eds.), *Modern and Ancient Fluvial Systems*, 6. *Int. Assoc. Sedimentol. Spec. Publ.* pp. 195–206.
- Franz, M., Nowak, K., Berner, U., Haunisch, C., Bandel, K., Rohling, H.G., Wolfgramm, M., 2014. Eustatic control on epicontinental basins: the example of the Stuttgart Formation in the central European Basin (Middle Keuper, late Triassic). *Glob. Planet. Change* 122, 305–329.
- Franz, M., Kustatscher, E., Heunisch, C., Niegel, S., Röhling, H.-G., 2019. The Schilfsandstein and its flora - arguments for a humid mid-Carnian episode? *J. Geol. Soc.* 176, 133–148. <https://doi.org/10.1144/jgs2018-053>.
- Furin, S., Preto, N., Rigo, M., Roghi, G., Giannola, P., Crowley, J.L., Bowring, S.A., 2006. High-precision U-Pb zircon age from the Triassic of Italy: implications for the Triassic time scale and the Carnian origin of calcareous nannoplankton and dinosaurs. *Geology* 34, 1009–1012.
- Gall, Q., Hyde, R., 1989. Analclime in lake and lake-margin sediments of the Carboniferous Rocky Brook Formation, Western Newfoundland, Canada. *Sedimentology* 36, 875–887. <https://doi.org/10.1111/j.1365-3091.1989.tb01751.x>.
- Gallego, O.F., Monferran, M.D., Stigall, A.L., Zacarías, I.A., Hegna, T.A., Jiménez, V.C., Bittencourt, J., Li, G., Barrios Calathaki, H.G., 2020. The Devonian-cretaceous fossil record of “conchostracans” of Africa and their paleobiogeographic relationships with other Gondwanan faunas. *J. Afr. Earth Sci.* <https://doi.org/10.1016/j.jafrearsci.2019.103648>.
- Geyer, O.F., Kelber, K.P., 2017. Spinicaudata (“Conchostraca”, Crustacea) from the Middle Keuper (Upper Triassic) of the southern Germanic Basin, with a review of Carnian-Norian taxa and suggested biozones. *Pal. Zeitsch* 92, 1–34. <https://doi.org/10.1007/s12542-017-0363-7>.
- Ghazy, S., Mountney, N.P., 2009. Facies and architectural element analysis of a meandering fluvial succession: the Permian Warchha Sandstone, Salt Range, Pakistan. *Sediment. Geol.* 221, 99–126.
- Golberg, K., Humayun, M., 2010. The applicability of the Chemical Index of Alteration as a paleoclimatic indicator: an example from the Permian of the Paraná Basin, Brazil. *Palaeogeogr. Palaeoclimatol. Palaeoecol.* 293, 175–183. <https://doi.org/10.1016/j.palaeo.2010.05.015>.
- Gulliford, A.R., Flint, S.S., Hodgson, D.M., 2017. Crevasse splay processes and deposits in an ancient distributive fluvial system: the lower Beaufort Group, South Africa. *Sediment. Geol.* 358, 1–18.
- Harding, A.G., Brown, R.H., 1974. Structural controls over thickness and facies distributions in Late Triassic-Early Jurassic carbonate-sulfate-redbeds sequence in southwestern Morocco, and its relationship to the opening of the Atlantic. *Geol. Soc. America, Abstr with programs* 7, 1099–1100.
- Hay, R.L., Sheppard, R.A., 2001. Occurrence of zeolites in sedimentary rocks: an overview. In: Bish, D., Ming, D. (Eds.), *Natural Zeolites: Occurrence, Properties, Applications, Reviews in Mineralogy*, 45. Mineralogical Society of America, Michigan, pp. 217–234.
- Hofmann, A., Tourani, A., Gaupp, R., 2000. Cyclicality of Triassic to lower Jurassic continental red beds of the Argana Valley, Morocco: implications for palaeoclimate and basin evolution. *Palaeogeogr. Palaeoclimatol. Palaeoecol.* 161, 229–266.
- Horne, J.C., Fern, J.C., 1976. Carboniferous Depositional Environments in the Pocahontas Basin, Eastern Kentucky and Southern West Virginia. Department of Geology, University South Carolina, Guidebook.
- Horton, T.W., Defliese, W.F., Tripathi, A.K., Oze, C., 2016. Evaporation induced 18O and 13C enrichment in lake systems: a global perspective on hydrologic balance effects. *Quat. Sci. Rev.* 131, 365–379. <https://doi.org/10.1016/j.quascirev.2015.06.030>.
- Hunt, A.P., Lucas, S.G., 1991. The Paleorhinus biochron and the correlation of the nonmarine Upper Triassic of Pangaea. *Paleontology* 34, 191–198.
- Iijima, A., 1980. *Geology of natural zeolites and zeolitic rocks*. Pure & Appl. Chem. 52, 2115–2130. Pergamon Press Ltd. Great Britain.
- Jalil, N.-E., Peyer, K., 2007. A new rauschianus (Archosauria, Suchia) from the Upper Triassic of the Argana Basin, Morocco. *Palaeontology* 50 (2), 417–430.
- Jalil, N.-E., 1999. Continental Permian and Triassic vertebrate localities from Algeria and Morocco and their stratigraphical correlations. *J. Afr. Earth Sci.* 29, 219–226.
- Jalil, N.-E., Dutuit, J.-M., 1996. Permian captorhinid reptiles from the Argana Formation, Morocco. *Palaeontology* 39, 907–918.
- Jalil, N.-E., Jenvier, P., Steyer, J.-S., 2009. A new cyclotosaurid (Amphibia, Temnospondyl) from the Triassic of Argana basin (High Atlas Mountains, Morocco); biostratigraphic implications: first International Congress on North African Vertebrate Palaeontology. Abstract 36–37.
- Jones, D.F., 1975. Stratigraphy, environments of deposition, petrology, age, and provenance of the basal redbeds of the Argana Valley, western High Atlas Mountains, Morocco. Ms Thesis. New Mexico Inst. Mining Technol., 148p.
- Kammerer, C.F., Nesbitt, S.J., Shubin, N.H., 2011. The first basal dinosauriform (Silesauridae) from the late Triassic of Morocco. *Acta Palaeontol. Pol.* 57 (2), 277–284.
- Kent, D.V., Olsen, P.E., Muttoni, G., 2017. Astrochronostratigraphic polarity time scale (APTS) for the late Triassic and early Jurassic from continental sediments and correlation with standard marine stages. *Earth Sci. Rev.* 166, 153–180.
- Klein, H., Voigt, S., Hminna, A., Saber, H., Schneider, J., Hmich, D., 2010. Early Triassic Archosaur-dominated footprint assemblage from the Argana Basin (Western High Atlas, Morocco). *Ichnos* 17, 215–227.
- Klein, H., Voigt, S., Saber, H., Schneider, J.W., Hminna, A., Fischer, J., Lagnaoui, A., Brosig, A., 2011. First occurrence of a Middle Triassic tetrapod Ichnofauna from the Argana Basin (Western High Atlas, Morocco). *Palaeogeogr. Palaeoclimatol. Palaeoecol.* 30, 218–231.
- Koch, P.L., 1998. Isotopic reconstruction of past continental environments. *Annu. Rev. Earth Pl. Sc.* 26, 573–613. <https://doi.org/10.1146/annurev.earth.26.1.573>.
- Kohn, M.J., 2010. Carbon isotope compositions of terrestrial C3 plants as indicators of (paleo)ecology and (paleo)climate. *Proc. Natl. Acad. Sci.* 107 (46), 19691–19695. <https://doi.org/10.1073/pnas.1004933107>.
- Kozur, H.W., 1982. Beiträge zur Taxonomie und stratigraphischen Auswertung der Untertriassischen Conchostracen. *Geologische und Paläontologische Mitteilungen Innsbruck* 11, 355–398.
- Kozur, H.W., Weems, R.E., 2010. The biostratigraphic importance of conchostracans in the continental Triassic of the northern hemisphere. In: Lucas, S.G. (Ed.), *The Triassic Timescale*, 334. Geological Society, London, pp. 315–417. Special Publications.
- Krystyn, L., 1978. Eine neue Zonengliederung im alpin-mediterranean Unterkarn. *Schriftenreihe Erdwis-senschaftlichen Österreichische Akademie der Wissenschaften* 4, 37–75.
- Lagnaoui, A., Klein, H., Saber, H., Fekkak, A., Belahmira, A., Schneider, J.W., 2016. New discoveries of archosaur and other tetrapod footprints from the Timezgadiouine Formation (Irohalene Member, Upper Triassic) of the Argana Basin, western High Atlas, Morocco – ichnotaxonomic implications. *Palaeogeogr. Palaeoclimatol. Palaeoecol.* 453, 1–9.
- Lagnaoui, A., Klein, H., Voigt, S., Hminna, A., Saber, H., Schneider, J.W., Werneburg, R., 2012. Late Triassic tetrapod-dominated ichnoassemblages from the Argana Basin (Western High Atlas, Morocco). *Ichnos* 19, 238–253.
- Lavielle, E., Piqué, A., 1992. La distension crustale atlantique et atlasiq ue au Maroc debut du Mésozoïque: le rejeu des structures hercyniennes. *Notes et M. Serv. Géol. Maroc. Rabat* 36, 343–357.
- Legarreta, L., Uliana, M.A., 1998. Anatomy of hinterland depositional sequences: Upper Cretaceous fluvial strata, Neuquen Basin, West-Central Argentina. In: Shanley, K.W., McCabe, P.J. (Eds.), *Relative Role of Eustasy, Climate, and Tectonism in Continental Rocks*, 59. SEPM Special Publication, pp. 83–107.
- Leleu, S., Hartley, A.J., van Oosterhout, C., Kennan, L., Ruckwied, K., Gerdes, K., 2016. Structural, stratigraphic and sedimentological characterization of a wide rift system: the Triassic rift system of the Central Atlantic Domain. *Earth Sci. Rev.* 158, 89–124.
- López-Gómez, J., De la Horra, R., Barrenechea, J., Borruel-Abadía, V., Martín-Chivelet, J., Juncal, M.A., Martín-González, F., Heredia, N., Díez, J., Buatois, L., 2021. Early Permian during the Variscan orogen collapse in the equatorial realm: insights from the Cantabrian Mountains (N Iberia) into climatic and environmental changes. *Int. J. Earth Sci.* 110, 1355–1387. <https://doi.org/10.1007/s00531-021-02020-0>.
- Lu, J., Zhang, P., Dal Corso, J., Yang, M., Wignall, P.B., Greene, S.E., Shao, L., Lyu, D., Hilton, J., 2021. Volcanically driven lacustrine ecosystem changes during the Carnian Pluvial Episode (Late Triassic). *PNAS* 118 (40), e2109895118.
- Lucas, S.G., 1998. Global Triassic tetrapod biostratigraphy and biochronology. *Palaeogeogr. Palaeoclimatol. Palaeoecol.* 143, 347–384.
- Lucas, S.G., 2010. The Triassic chronostratigraphic scale: history and status. In: Lucas, S. G. (Ed.), *The Triassic Timescale*, 334. Geological Society, pp. 17–40. Special Publication.
- Lucas, S.G., 2018. Late Triassic terrestrial tetrapods: biostratigraphy, biochronology and biotic events. In: Tanner, L.H. (Ed.), *The late Triassic World, Topics in Geobiology*. Springer International Publishing, p. 46. https://doi.org/10.1007/978-3-319-68009-5_10.
- Machette, M.N., 1985. Calcic soils of the southwestern United States. In: Weide, D.L. (Ed.), *Soils and Quaternary Geology of the Southwestern United States*, pp. 10–21. Special Paper of the Geological Society of America 203.
- Mack, G.H., James, W.C., Monger, H.C., 1993. Classification of paleosols. *Geol. Soc. Am. Bull.* 105, 129–136. [https://doi.org/10.1130/0016-7606\(1993\)105<0129:COP>2.3.CO;2](https://doi.org/10.1130/0016-7606(1993)105<0129:COP>2.3.CO;2).
- Mader, N.K., Redfern, J., 2011. A sedimentological model for the continental Upper Triassic Tadrat Ouadou Sandstone Member: recording an interplay of climate and tectonics (Argana valley, SW Morocco). *Sedimentology* 58 (5), 1247–1282.
- Mader, N.K., Redfern, J., El Ouataoui, M., 2017. Sedimentology of the Essaouira Basin (Meskala Field) in context of regional sediment distribution patterns during upper Triassic pluvial events. *J. Afr. Earth Sci.* 130, 293–318.
- Mancuso, A.C., Benavente, C.A., Irmis, R.B., Mundil, R., 2020. Evidence for the Carnian Pluvial Episode in Gondwana: New multiproxy climate records and their bearing on early dinosaur diversification. *Gondwana* 86, 104–125. <https://doi.org/10.1016/j.gr.2020.05.009>.
- Mancuso, A.C., Irmis, R.B., Pedernera, T.E., Gaetano, L.C., Benavente, C.A., Breeden III, B.T., 2022. Paleoenvironmental and Biotic Changes in the Late Triassic of Argentina: Testing Hypotheses of Abiotic Forcing at the Basin Scale. *Front. Earth Sci.* 10, 1–28. <https://doi.org/10.3389/feart.2022.883788>.

- Manspeizer, W., Puffer, J.H., Cousminer, H.L., 1978. Separation of Morocco and eastern North America: A Triassic-Liassic stratigraphic record. *Geol. Soc. Am. Bull.* 89, 901–920.
- Martens, T., 2012. Biostratigraphie der Conchostraca (Branchiopoda, Crustacea) de Rotliegend. Hrsg.; Koordination und Redaktion. In: Lutzner, H., Kowalczyk, G. (Eds.), *Stratigraphie von Deutschland X. Rotliegend. Teil I: Innervariatische Becken. – Schriftenreihe der Deutschen Gesellschaft für Geowissenschaften, Heft 61. Deutsche Stratigraphische Kommission*, pp. 98–109 für die Subkommission Perm-Trias.
- Maynard, J.B., 1992. Chemistry of modern soils as a guide to interpreting Precambrian paleosols. *J. Geol.* 100, 279–289. <https://doi.org/10.1086/629632>.
- McCahon, T.J., Miller, K.B., 1997. Climatic significance of natic horizons in Permian (Asselian) paleosols of north Central Kansas, U.S.A. *Sedimentology* 44, 113–125. <https://doi.org/10.1111/j.1365-3091.1997.tb00427.x>.
- Medina, F., 1995. Syn- and postrift evolution of the El Jadida-Agadir basin (Morocco): constraints for the rifting models of the Central Atlantic. *Can. J. Earth Sci.* 32, 1273–1291.
- Medina, F., Tourani, A., Benaouiss, N., Jalil, N., 2000. Le Permien Supérieur et le Trias du bassin d'Argana. *Livret guide 1st Journée, excursion de l'AGP-GMPT*, 17p.
- Mercuzot, M., Bourquin, S., Pellenard, P., Beccaletto, L., Schnyder, J., Baudin, F., Ducassou, C., Garel, S., Gand, G., 2022. Reconsidering Carboniferous-Permian continental paleoenvironments in eastern equatorial Pangea: facies and sequence stratigraphy investigations in the Autun Basin (France). *Int. J. Earth Sci.* 1–34.
- Miall, A.D., 1996. The Geology of Fluvial Deposits. In: *Sedimentary Facies, Basin Analysis and Petroleum Geology*. Springer, Berlin, p. 582 p.
- Miall, A.D., 2014. In: *Fluvial Depositional Systems*. Springer, Berlin, p. 316.
- Michel, L.A., Tabor, N.J., Montañez, I.P., Schmitz, M.D., Davydov, V.I., 2015. Chronostratigraphy and Palaeoclimatology of the Lodeve Basin, France: evidence for a pan-tropical aridification event across the Carboniferous-Permian boundary. *Palaeogeogr. Palaeoclimatol. Palaeoecol.* 430, 118–131.
- Montañez, I., Tabor, N., Niemeier, D., Dimichele, W., Frank, T., Fielding, C., Isbell, J., Birgenheier, L., Rygel, M., 2007. CO₂-Forced climate and Vegetation Instability during late Paleozoic Deglaciation. *Science* 315, 87–91. <https://doi.org/10.1126/science.1134207>.
- Moore, D.M., Reynolds Jr., R.C., 1989. *X-Ray Diffraction and the Identification and Analysis of Clay Minerals*. Oxford University Press, Oxford.
- Müller, A.B., Strauss, H., Hartkopf-Fröder, C., Littke, R., 2006. Reconstructing the evolution of the latest Pennsylvanian–earliest Permian Lake Odernheim based on stable isotope geochemistry and palynofacies: A case study from the Saar-Nahe Basin, Germany. *Palaeogeogr. Palaeoclimatol. Palaeoecol.* 240 (1–2), 204–224. <https://doi.org/10.1016/j.palaeo.2006.03.049>.
- Nesbitt, H.W., Young, G.M., 1982. Early Proterozoic climates and plate motions inferred from major element chemistry of lutites. *Nature* 299, 715–717.
- Nordt, L., Driese, S.G., 2009. Hydropedological model of vertisol formation along the Gulf Coast Prairie land resource area of Texas. *Hydrol. Earth Syst. Sci.* 13, 2039–2053. <https://doi.org/10.5194/hess-13-2039-2009>.
- Nordt, L., Wilding, L., Lynn, W.L., Crawford, C., 2004. Vertisol genesis in a humid climate in the coastal plain of Texas. *Geoderma* 122, 83–102. <https://doi.org/10.1016/j.geoderma.2004.01.020>.
- Olsen, P.E., Kent, D.V., Et-Touhami, M., Puffer, J., 2003. Cyclo-, magneto-, and biostratigraphic constraints on the duration of the CAMP event and its relationship to the Triassic-Jurassic Boundary. In: Hames, W.E., McHone, J.G., Renne, P.R., Ruppel, C. (Eds.), *The Central Atlantic Magmatic Province: Insights from Fragments of Pangea*. American Geophysical Union, Washington, DC, pp. 7–32.
- Piqué, A., Le Roy, P., Amrhar, M., 1998. Transtensive synsedimentary tectonics associated with ocean opening: the Essaouira-Agadir segment of the Moroccan Atlantic margin. *J. Geol. Soc. Lond.* 155, 913–928.
- Preto, N., Kustatscher, E., Wignall, P., 2010. Triassic climates – State of art. *Palaeogeogr. Palaeoclimatol. Palaeoecol.* 290, 1–10.
- Preto, N., Hinnov, L.A., 2003. Unraveling the origin of carbonate platform cyclothem in the Upper Triassic Dürresstein Formation (Dolomites, Italy). *J. Sediment. Res.* 73, 774–789.
- Puigdefàbregas, C., van Vliet, A., 1978. Meandering stream deposits from the Tertiary of the southern Pyrenees. In: Miall, A.D. (Ed.), *Fluvial Sedimentology*, 5. Can. Soc. Petrol. Geol. Mem., pp. 469–485.
- Redfern, J., Shannon, P.M., Williams, B.P.J., Tyrrell, S., Leleu, S., Fabuel-Pérez, I., Baudon, C., Stolfova, K., Hodgetts, D., van Lanen, X., Speksnijder, A., Haughton, P.D. W., Daly, J.S., 2010. An integrated study of Permo-Triassic basins along the North Atlantic passive margin: implication for future exploration. *Geol. Soc. Lond. Petrol. Geol. Conf. Ser.* 7, 921–936.
- Retallack, G.J., 1988. Field recognition of paleosols. In: Reinhardt, J., Sigleo, W.R. (Eds.), *Paleosols and Applications*, 216, pp. 1–21. Geological Society of America Special Paper.
- Retallack, G.J., 2001. *Soils of the Past*. Blackwell, Oxford, 404p.
- Roghi, G., Gianolla, P., Minarelli, L., Pilati, C., Preto, N., 2010. Palynological correlation of Carnian humid pulses throughout the western Tethys. *Palaeogeogr. Palaeoclimatol. Palaeoecol.* 290, 89–106.
- Roghi, G., Gianolla, P., Kustatscher, E., Schmidt, A.R., Seyfullah, L.J., 2022. An Exceptionally Preserved Terrestrial Record of LIP Effects on Plants in the Carnian (Upper Triassic) Amber-Bearing Section of the Dolomites, Italy. *Front. Earth Sci.* 10, 900586.
- Royer, D.L., Berner, R.A., Montañez, I.P., Tabor, N.J., Beerling, D.J., 2004. CO₂ as the primary driver of Phanerozoic climate. *GSA Today* 14, 1–10.
- Saber, H., El Wartiti, M., Broutin, J., 2001. Dynamic sedimentology of two Upper Stephano-lower Permian basins: ida Ou Zal and Ida Ou Ziki, western High Atlas, Morocco. *J. Afr. Earth Sci.* 32, 573–594.
- Saber, H., El Wartiti, M., Hmich, D., Schneider, J.W., 2007. Tectonic evolution from the Hercynian shortening to the Triassic extension in the Paleozoic Western High Atlas (Morocco). *J. Iber. Geol.* 33 (1), 31–40.
- Schneider, J.W., Scholze, F., 2018. Late Pennsylvanian–Early Triassic conchostracan biostratigraphy: a preliminary approach. In: Lucas, S.G., Shen, S.Z. (Eds.), *The Permian Timescale*, vol. 450. Geol. Soc., London, Spec. Publ., pp. 365–386. <https://doi.org/10.1144/SP450.6>. 2016.
- Scholze, F., Golubev, V.K., Niedzwiedzki, G., Schneider, J.W., Sennikov, A.G., 2018. Late Permian conchostracans (Crustacea, Branchiopoda) from continental deposits in the Moscow syncline, Russia. *J. Paleontol.* 93 (1), 72–97. <https://doi.org/10.1017/jpa.2018.58>.
- Scholze, F., Schneider, J.W., 2015. Improved method-ology of 'conchostracan' (Crustacea: Branchiopoda) classification for biostratigraphy. *Newsl. Stratigr.* 48, 287–298.
- Scholze, F., Schneider, J.W., Werneburg, R., 2016. Conchostracans in continental deposits of the Zechstein-Buntsandstein transition in Central Germany: taxonomy and biostratigraphic implications for the position of the Permian-Triassic boundary within the Zechstein Group. *Palaeogeogr. Palaeoclimatol. Palaeoecol.* 449, 174–193.
- Schulze, D.G., 2005. *Clay minerals*. In: Hillel, Daniel (Ed.), *Encyclopedia of Soils in the Environment*. Elsevier, pp. 246–254. <https://doi.org/10.1016/B0-12-348530-4/00189-2>.
- Schumm, S.A., 1977. *The Fluvial System*. Wiley, New York.
- Sheldon, N.D., Tabor, N.J., 2009. Quantitative Paleoenvironmental and Paleoclimatic Reconstruction using Paleosols. *Earth Sci. Rev.* 95, 1–52. <https://doi.org/10.1016/j.earscirev.2009.03.004>.
- Sheldon, N.D., Retallack, G.J., Tanaka, S., 2002. Geochemical climofunctions from North America soils and application to paleosols across the Eocene-Oligocene boundary in Oregon. *J. Geol.* 110, 687–696. <https://doi.org/10.1086/342865>.
- Sikes, N.E., Ashley, G.M., 2007. Stable isotopes of pedogenic carbonates as indicators of paleoecology in the Plio-Pleistocene (upper Bed I), western margin of the Olduvai Basin, Tanzania. *J. Hum. Evol.* 53, 574–594. <https://doi.org/10.1016/j.jhevol.2006.12.008>.
- Simms, M.J., Ruffell, A.H., 1989. Synchronicity of climatic change and extinctions in the late Triassic. *Geology* 17, 265–268.
- Simon, S.S.T., Gibling, M.R., 2017. Fine-grained meandering systems of the lower Permian Clear Fork Formation of north-Central Texas, AUA: Lateral and oblique accretion on an arid plain. *Sedimentology* 64, 714–746.
- Smith, N.D., Cross, T.A., Dufficy, J.P., Clough, S.R., 1989. Anatomy of an avulsion. *Sedimentology* 36, 1–23.
- Soil Survey Staff, 1999. *Soil Taxonomy: A basic system of soil classification for making and interpreting soil surveys*. In: *Agricultural Handbook 436, Natural Resources Conservation Service, 2nd edition*. USDA, Washington DC, USA, p. 869.
- Stefani, M., Furin, S., Gianolla, P., 2010. The changing climate framework and depositional dynamics of the Triassic carbonate platforms from the Dolomites. *Palaeogeogr. Palaeoclimatol. Palaeoecol.* 290, 43–57.
- Sun, Y.D., Wignall, P.B., Joachimski, M.M., Bond, D.P.G., Grasby, S.E., Lai, X.L., Wang, L. H., Zang, Z.T., Sun, S., 2016. Climate warming, euxinia and carbon isotope perturbations during the Carnian (Triassic) Crisis in China. *Earth Planet. Sci. Lett.* 444, 88–100.
- Surdam, R.C., Sheppard, R.A., 1978. Zeolites in saline, alkaline-lake deposits. In: Sand, L. B., Humpton, F.A. (Eds.), *Natural Zeolites Occurrence, Properties*. Pergamon Press, Use.
- Tabor, N.J., Myers, T.S., 2015. Paleosols as Indicators of Paleoenvironment and Paleoclimatic. *Annu. Rev. Earth Planet. Sci.* 43, 333–361. <https://doi.org/10.1146/annurev-earth-060614-105355>.
- Tabor, N.J., Myers, T.S., Sidor, C.A., Smith, R.M.H., Nesbitt, S.J., Angielczyk, K., 2017. Paleosols of the Permian-Triassic: proxies for rainfall, climate change and major changes in terrestrial tetrapod diversity. *J. Vertebr. Paleontol.* 37, 240–253. <https://doi.org/10.1080/02724634.2017.1415211>.
- Talbot, M.R., 1990. A review of the paleohydrological interpretation of carbon and oxygen isotopic ratios in primary lacustrine carbonates. *Chem. Geol. Isotope Geosci. Section* 80, 261–279. [https://doi.org/10.1016/0168-9622\(90\)90009-2](https://doi.org/10.1016/0168-9622(90)90009-2).
- Tomimatsu, Y., Nozaki, T., Sato, H., Takaya, Y., Kimura, J.-I., Chang, Q., Naraoka, H., Rigo, M., Onoue, T., 2021. Marine osmium isotope record during the Carnian pluvial episode (Late Triassic) in the pelagic Panthalassa Ocean. *Glob. Planet. Chang.* 197, 103387.
- Tixeront, M., 1973. Lithostratigraphie et minéralisation cuprifères et uranifères stratiformes syngénétiques et familiaires des formations détritiques permotriassiques du Couloir d'Argana (Haut-Atlas occidental, Maroc). *Notes Mém. Serv. Géol. Maroc* 249, 147–177.
- Tourani, A., Lund, J.J., Benaouiss, N., Gaupp, R., 2000. Stratigraphy and Triassic syn-rift deposition in Western Morocco. *Zbl. Geol. Paläontol.* 1 (9–10), 1193–1215.
- Tourani, A., Benaouiss, N., Gand, G., Bourquin, S., Jalil, N.-E., Broutin, J., Battail, B., Germain, D., Khaldoune, F., Sebban, S., Steyer, J.-S., Vacant, R., 2010. Evidence of an early Triassic age (Olenekian) in Argana Basin (High Atlas, Morocco) based on new chirotheriid traces. *Compt. Rend. Palevol.* 9, 201–208.
- Verati, C., Rapaille, C., Féraud, G., Marzoli, A., Bertrand, H., Youbi, N., 2007. 40Ar/39Ar ages and duration of the Central Atlantic magmatic province volcanism in Morocco and Portugal and its relation to the Triassic-Jurassic boundary. *Palaeogeogr. Palaeoclimatol. Palaeoecol.* 244 (1–4), 308–325.
- Whiteside, J.H., Olsen, P.E., Kent, D.V., Fowell, S.J., Et-Touhami, M., 2007. Synchrony between the Central Atlantic Magmatic Province and the Triassic-Jurassic mass-extinction event? *Palaeogeogr. Palaeoclimatol. Palaeoecol.* 244, 345–367.
- Willis, B.J., Behrensmeier, A.K., 1994. Architecture of Miocene overbank deposits in the northern Pakistan. *J. Sediment. Res.* B64, 60–67.

- Wood, J.M., 1989. Alluvial architecture of the Upper Cretaceous Judith River Formation, Dinosaur Provincial Park, Alberta, Canada. *Bull. Can. Petrol. Geol.* 37, 169–181.
- Wu, C., Ullah, M., Lu, J., Bhattacharya, J.P., 2016. Formation of point bars through rising and falling flood stages: evidence from bar morphology, sediment transport and bed shear stress. *Sedimentology* 63, 1458–1473.
- Zhang, W.T., Chen, P.J., Shen, Y.B., 1976. Fossil Conchostraca of China. Science Press, p. 325.
- Zouheir, T., Hminna, A., Klein, H., Lagnaoui, A., Saber, H., Schneider, J.W., 2018. Tetrapod footprints from the late Triassic of Irohalene (Argana Basin, Western High Atlas, Morocco) - most recent update and paleoenvironmental implications. In: *Second International Congress on Permian and Triassic*. April 25–27, Casablanca (Morocco), pp. 55–56.
- Zouheir, T., Hminna, A., Klein, H., Lagnaoui, A., Saber, H., Schneider, J.W., 2020. Unusual archosaur trackway and associated tetrapod ichnofauna from Irohalene member (Tizezgadiouine formation, late Triassic, Carnian) of the Argana Basin, Western High Atlas, Morocco. *Hist. Biol.* 32, 589–601.
- Zouheir, T., Hminna, A., Saber, H., Klein, H., Lagnaoui, A., Voigt, S., Rmich, A., Schneider, J.W., Lucas, S.G., 2023. Ichnodiversity and facies of Triassic red beds in the Irohalene area (Argana Basin, Western High Atlas, Morocco): implications for palaeoenvironment. *Hist. Biol.* 35 (6), 875–908. <https://doi.org/10.1080/08912963.2022.2069018>.